Global Sensitivity Analysis of simulated polarimetric remote sensing observations over snow

Matteo Ottaviani[1,2], Gabriel H. Myers[3], Nan Chen[4]

[1]NASA Goddard Institute for Space Studies, New York, NY 10025, USA
[2]Terra Research Inc, Hoboken, NJ 07030, USA
[3]Courant Institute of Mathematical Sciences, New York University, New York, NY 10012, USA
[4]Stevens Institute of Technology, Hoboken, NJ 07030, USA

Correspondence to: Matteo Ottaviani (matteo.ottaviani@nasa.gov)

Abstract. This study presents a detailed theoretical assessment of the information content of passive polarimetric observations over snow scenes, using a Global Sensitivity Analysis (GSA) method. Conventional sensitivity studies focus on varying a single parameter while keeping all other parameters fixed. In contrast, the GSA correctly addresses the covariance of state parameters across their entire parameter space, hence favoring a more correct interpretation of inversion algorithms and the optimal design of their state vectors.

The forward simulations exploit a vector radiative transfer model to obtain the Stokes vector emerging at the top of the atmosphere for different solar zenith angles, when the bottom boundary consists of a vertically resolved snowpack of non-spherical grains. The presence of light-absorbing particulates (LAPs), either embedded in the snow or aloft in the atmosphere above in the form of aerosols, is also considered. The results are presented for a set of wavelengths spanning the visible (VIS), near-infrared (NIR), and short-wave infrared (SWIR) region of the spectrum.

The GSA correctly captures the expected, high sensitivity of the total reflectance to LAPs in the VIS-NIR, and to grain size at different depths in the snowpack in the NIR-SWIR. Provided adequate viewing geometries, mono-angle measurements of total reflectance in the VIS-SWIR (akin to those of the Moderate Resolution Imaging Spectroradiometer, MODIS) resolve grain size in the top layer of the snowpack sufficiently well. The addition of multi-angle polarimetric observations in the VIS-NIR provides information on grain shape and microscale roughness. The simultaneous sensitivity in the VIS-NIR to both aerosols and snow-embedded impurities can be disentangled by extending the spectral range to the SWIR, which contains information on aerosol optical depth while remaining essentially unaffected when the same particulates are mixed with the snow. Multi-angle polarimetric observations can therefore (i) effectively partition LAPs between the atmosphere and the surface, which represents a notorious challenge for snow remote sensing based on measurements of total reflectance only; and (ii) lead to better estimates of grain shape and ice crystal roughness, and in turn of the asymmetry parameter which is critical for the determination of albedo. The retrieval uncertainties are minimized when the Degree of Linear Polarization is used in place of the polarized reflectance.

The Sobol indices, main metric for the GSA, were used to inform on the choice of state parameters in retrievals performed on data simulated for multiple instrument configurations. Improvements in retrieval quality with added measurements and channels reflect the information content identified by the Sobol indices.

The results encourage the development of new remote sensing algorithms that fully leverage multi-angle and polarimetric capabilities of modern remote sensors. They can also aid flight planning activities, since the optimal exploitation of the information content of multi-angle measurements depends on the viewing geometry. The better characterization of surface and atmospheric parameters in snow-covered regions advances the research opportunities for scientists of the cryosphere, and ultimately benefits albedo estimates in climate models.

1 Introduction

The quantification of the surface energy balance of snow-covered regions is of extreme importance for Earth-system models simulations aimed at global climate studies (Hansen and Nazarenko, 2004; Fettweis et al., 2008; van den Broeke et al., 2011; Rae et al., 2012; Van Angelen et al., 2012; Tedesco et al., 2013; Alexander et al., 2014; Colgan et al., 2014). Since snow albedo fundamentally depends on the optical and microphysical properties of the ice crystals (Wiscombe and Warren, 1980; Aoki et al., 2000; Flanner and Zender, 2006; Bougamont et al., 2007; Dang et al., 2016; He et al., 2018) and of light-absorbing impurities potentially present in the snowpack (Warren and Wiscombe, 1980; Hansen and Nazarenko, 2004; Dumont et al., 2014), a better knowledge of the properties of such components and their evolution is a high priority objective for the modeling of the cryosphere (Tedesco et al., 2013; Dumont et al., 2014).

One source of uncertainty in the remote sensing of these properties is the treatment of snow as a collection of spherical grains (Tanikawa et al., 2019). Although useful in some contexts, such approximation can underestimate the albedo by a few percent (Xie et al., 2006; Tedesco and Kokhanovsky, 2007; Libois et al., 2013; Tedesco et al., 2013; Dumont et al., 2014; Dang et al., 2016; Räisänen et al., 2017), a discrepancy that can be exaggerated by snow albedo feedback processes (Thackeray, 2018; Colman, 2013; Hansen and Nazarenko, 2004). To avoid this assumption we employ hexagonal prisms, which have been demonstrated (van Diedenhoven et al., 2012) to serve well as radiative proxies for more complex shapes, while having the advantage of being characterized only by their Aspect Ratio (AR, with AR>1 for columns and AR<1 for plates) and the microscale roughness (D) of the crystal facets. The implementation of this methodology in advanced radiative transfer (RT) models has produced successful retrievals for parameters descriptive of the crystals forming ice clouds (van Diedenhoven et al., 2014b) and the reflectance properties of snow-covered surfaces (Ottaviani et al., 2012; 2015) from data collected with the NASA Goddard Institute for Space Studies (GISS) airborne Research Scanning Polarimeter (RSP; Cairns et al., 1999).

Another major challenge is the determination of light-absorbing particulate (LAP) content and its partitioning between those deposited in snow versus those suspended above in the form of atmospheric aerosols (Warren, 2013). Because the polarization state of light is also sensitive to the vertical partitioning of LAPs between the snowpack and the atmosphere

(Ottaviani, 2022), remote sensors like the RSP, the Second Generation Global Imager (SGLI, Tanaka et al., 2018), the polarimeters launched aboard the Plankton, Aerosol, Cloud, ocean Ecosystem (PACE) mission (McBride et al., 2023; Hasekamp et al., 2018), and the upcoming Multi-view Multi-channel Multi-polarization Imaging (3MI) mission (Biron et. al., 2013; Marbach et. al., 2013) offer augmented retrieval capabilities.

Zhang et. al. (2023) have recently evaluated the performance of introducing a snow kernel in an inverse algorithm to retrieve the microphysics of aerosols above snow based on observations of the Polarization and Directionality of the Earth's Reflectances (POLDER) spaceborne sensor, that flew from 2004 to 2013. However, their study does not address the retrieval of the microphysical properties of the snowpack and the distribution of LAPs between the snow and the atmosphere, or information content aspects. This paper extends the studies presented in Ottaviani (2022), examining these details via a Global Sensitivity Analysis (GSA) of simulated top-of-the-atmosphere (TOA) polarimetric observations.

Section 2 explains the setup of the RT calculations needed to generate the look-up table (LUT) of the Stokes vectors at the TOA produced for random combinations of the input parameters and outlines the adaptation of the GSA formalism to the scopes of this analysis. The results of the GSA are presented in Sec. 3 along with inverse retrievals of spaceborne observations simulated for different observational configurations. We first consider pure-snow scenes to highlight the sensitivity to the ice crystal properties. We then address more realistic remote sensing scenarios where the atmosphere is allowed to contain a layer of absorbing aerosols and the snowpack contains impurities. The paper concludes with some recommendations for operational retrievals.

2 Methods

2.1 Radiative Transfer Simulations

The plane-parallel RT code employed to generate the LUT is based on the general doubling-adding formalism described by De Haan et al. (1987). It features a consistent treatment of the radiative effects deriving from atmospheric molecular scattering, aerosols and clouds, and any surface whose reflectance is known in analytical form or in terms of its Bidirectional Reflectance Distribution Function (BRDF) properties and the polarization counterpart (BPDF). The code has been used for decades to model measurements from the RSP over a variety of Earth scenes, including those containing ice crystals in clouds (van Diedenhoven et al., 2013) and ground snow (Ottaviani et al., 2012; 2015).

Recognizing the similarities with the polarimetric signatures of ice crystals in cirrus clouds (Ottaviani et al., 2012; 2015), the snowpack is modeled as an optically semi-infinite collection of non-spherical ice crystals at the bottom of the atmosphere, so that the reflectance of the actual underlying surface is irrelevant. As with other media, the photon penetration depth in snow depends on wavelength (Kokhanovsky, 2022; Libois et al., 2013), so different instrumental channels effectively probe different depths, and this fact must be taken into account during multi-spectral retrievals (Li et al., 2001). In contrast to retrievals of grain size for mono-layer snowpacks (Nolin and Dozier, 1993; Painter et al., 2003), such an approach has been exploited to retrieve grain size in both a thin surface layer and a thick layer below using measurements

from MODIS (Aoki et al., 2007; Painter et al., 2009). For this reason, the snowpack in our model is vertically resolved in a thick bottom layer capped by a thin top layer (see Fig. 1).

To span a wide spectral range as required by remote sensing applications, we consider channels at 411, 469, 555, 670, 864, 1589 and 2266 nm, which in the case of the RSP sensor are all equipped with polarization capabilities. Except for minimal differences in the precise centerband values, the channels in this set are also available from heritage instruments like e.g. the Moderate Resolution Imaging Spectroradiometer (MODIS), but in total reflectance and at one angle only for each pixel to provide information on the atmospheric correction both over land and ocean. We include in the list of channels the MODIS band at 2112 nm despite it being very close to 2266 nm, because these wavelengths lie on the shoulder of a major absorption band where radiative differences can arise very quickly. Moreover, this channel will be available from 3MI with polarization capabilities.

Absorbing aerosols are climatologically relevant because deposition events can cause large variations in albedo (Dumont et al., 2014; Hansen and Nazarenko, 2004; Khan et. al., 2023; Warren and Wiscombe, 1980). To examine the capability of different observational configurations (see Sect. 3) to distinguish them from impurities in the snow, both the lowest atmospheric layer (located within the first 2 km above the snowpack) and the snow are allowed to contain variable amounts of the same spherical LAP with properties typical of soot (n = 1.80 - 0.6i, r_{eff} = 0.11 μm, v_{eff} = 0.38) (Dubovik et al., 2002).

Finally, the presence of exclusively absorbing gases (H_2O, O_3, etc.) in the background atmosphere is neglected, because it does not affect the conclusions drawn from the sensitivity study presented below. The complete list of the descriptive parameters and their bounds in the LUT can be found in Table 1.

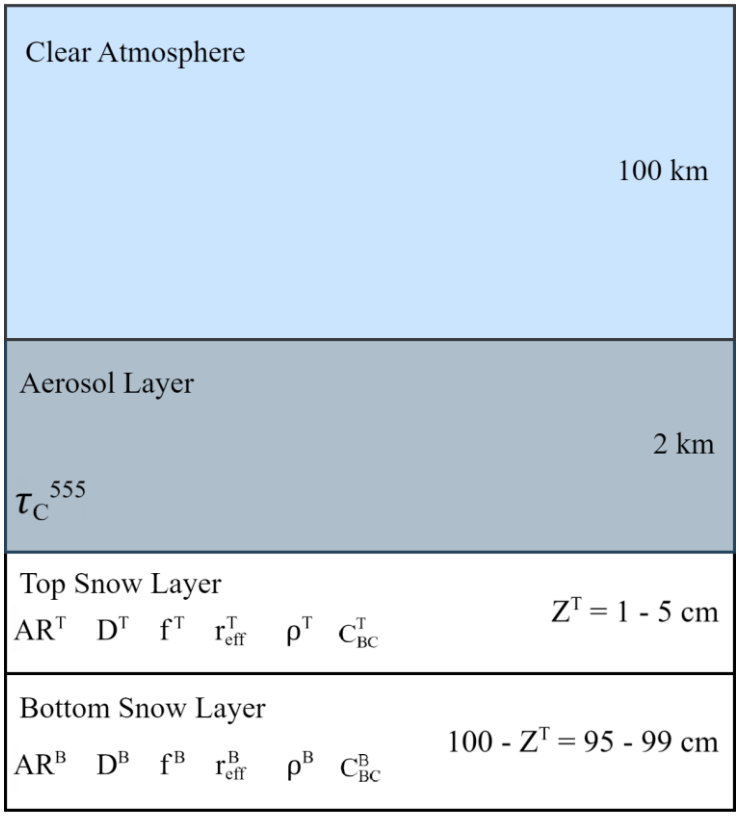

Figure 1: Model for the snow-atmosphere system. The snowpack is described by a thin layer sitting over an optically semi-infinite layer, for a total thickness of 1 m. The parameters in each layer are varied independently. The atmosphere is allowed to contain light-absorbing aerosols (τ_c^{555}) in the lowest layer (first 2 km above the surface). See Table 1 for the complete list of model parameters and their ranges of variability.

Parameter	***Symbol***	***Bounds***
Aspect Ratio	AR^T, AR^B	0.037 - 1.0
Microscale Roughness	D^T, D^B	0.2 - 0.7
Snow Grain Mixing Proportion (area fraction of columns)	f^T, f^B	0.0 - 1.0
Snow Grain Effective Radius	r_{eff}^T, r_{eff}^B	56 - 2560 μm
Top Layer Snow Density	ρ^T	0.07 - 0.4 g/cm^3
Bottom Layer Snow Density	ρ^B	0.25 - 0.5 g/cm^3
LAP Concentration in Snow	C_{BC}^T, C_{BC}^B	0 - 1 ppmw
Aerosol Optical Depth (555 nm)	τ_c^{555}	0.0 - 0.4
Top Layer Thickness	Z^T	0.01 - 0.05 m

Table 1: Model parameters and their lower/upper bounds. The parameters describing the top and bottom snow layer are denoted with superscripts T and B, and are varied independently. Soot-like LAPs are characterized by n = 1.80 - 0.6i, r_{eff} = 0.11 μm, and v_{eff} = 0.38 (Dubovik et al., 2002; Torres et al. 2017).

The optical properties of the hexagonal prisms are produced via a Geometric Optics (GO) code (Macke et al., 1996; van Diedenhoven et al., 2012) as a function of aspect ratio (AR), microscale roughness (D), and effective radius (r_{eff}), and are integrated over a power-law size distribution (Geogdzhayev and van Diedenhoven, 2016). The microscale roughness represents the standard deviation of the distribution of angles used to randomly perturb the orientation of the ice crystal facet encountered by the incident beam in the GO calculations (van Diedenhoven et al., 2014a). Previous attempts to fit the surface contribution to the signal measured by airborne polarimeters show that D≳0.25 (Ottaviani, 2012; 2015). Such roughness is sufficient to extinguish the halo peaks characteristic of more pristine crystals (van Diedenhoven et al., 2012).

The asymmetry parameter of columns and plates of reciprocal ARs are very similar (Ottaviani, 2015; van Diedenhoven et al., 2014a). To enable retrievals of representative crystal shapes and test the sensitivity to the mixing proportion, we therefore assume that the population of grains is composed of a fraction *f* of plates (superscript 'P') with aspect ratio AR^P and a fraction (1-*f*) of columns (superscript 'C') with aspect ratio $AR^C=1/AR^P$. The fraction is allowed to vary independently in each layer. For ice crystals of a given AR, the extinction and scattering efficiencies are:

$$Q_{ext} = \frac{C_{ext}}{A} \quad (1)$$

$$Q_{sca} = \frac{C_{sca}}{A} \quad (2)$$

Where C_{ext}, C_{sca} are the extinction and scattering coefficient, and A is the projected area of the hexagonal prism (van Diedenhoven et al., 2014a). The extinction and scattering efficiencies of the mixture are:

$$Q_{\text{ext}}^{\text{mix}} = f \cdot Q_{\text{ext}}^{C} + (1-f) \cdot Q_{\text{ext}}^{P} \quad (3)$$

$$Q_{\text{sca}}^{\text{mix}} = f \cdot Q_{\text{sca}}^{C} + (1-f) \cdot Q_{\text{sca}}^{P} \quad (4)$$

and the corresponding phase function and asymmetry parameter are:

$$P^{mix} = (f \cdot P^{C} \cdot Q_{sca}^{C} + (1-f) \cdot P^{P} \cdot Q_{sca}^{P}) \,/\, Q_{sca}^{\text{mix}} \quad (5)$$

$$g^{mix} = (f \cdot g^{C} \cdot Q_{sca}^{C} + (1-f) \cdot g^{P} \cdot Q_{sca}^{P}) \,/\, Q_{sca}^{mix} \quad (6)$$

The projected area of the mixture is assumed to be that of the column crystals, so that the extinction cross section, the scattering cross section and the single scattering albedo of the mixture are:

$$C_{ext}^{mix} = Q_{ext}^{mix} \cdot A^{C} \quad (7)$$

$$C_{sca}^{mix} = Q_{sca}^{mix} \cdot A^{C} \quad (8)$$

$$SSA^{mix} = Q_{sca}^{mix} \,/\, Q_{ext}^{mix} \quad (9)$$

The impurities in the snowpack are externally mixed to the snow grains (Tanikawa et al., 2019). Their optical properties are calculated by Mie calculations internal to the RT code, as done for the aerosols, and are assumed to follow lognormal aerosol size distributions (Hansen and Travis, 1974). Using the layer-resolved inherent optical properties above, together with the optical depths, the RT Code simulates the TOA reflectances (R_I, R_Q, R_U) corresponding to the first three parameters (I , Q, U) of the Stokes vector, describing the linear state of light polarization. Circular polarization is represented by the fourth element (V), which has generally negligible relevance to remote sensing applications (Kawata, 1978), so it is omitted from the analysis. The modelled reflectances can be output for any viewing geometry. We choose observations along the principal-plane for which the range of the collected scattering angles is maximized.

The GSA considers the total reflectance (R_I), the polarized reflectance ($R_p = \sqrt{R_U^2 + R_Q^2}$), and also the degree of linear polarization (DoLP = R_p/R_I), which in RSP-like instruments is measured at a much higher accuracy than R_p (Knobelspiesse et al., 2012; Cairns et al., 1999).

2.2 Global Sensitivity Analysis Formalism

To illustrate the pitfalls of conventional sensitivity studies applied to hyperdimensional state spaces, Fig. 2 shows the sensitivity of R_I, R_p, and DoLP to AR^T in the SWIR (cf. Ottaviani, 2022), for two different values of r_{eff}^T. For r_{eff}^T=1280 μm (solid lines) the signals are essentially unaffected by variations in AR^T; conversely, detectable differences arise for r_{eff}^T=56 μm (dashed lines). Similarly the DoLP grows with r_{eff}^T, but only for small radii are the curves for the two ARs

distinguishable. Because the sensitivity to AR^T depends on r_{eff}^T, and that of any parameter can similarly depend on the set of all other values kept fixed, it is necessary to use a method like the GSA to properly quantify the information content of the model.

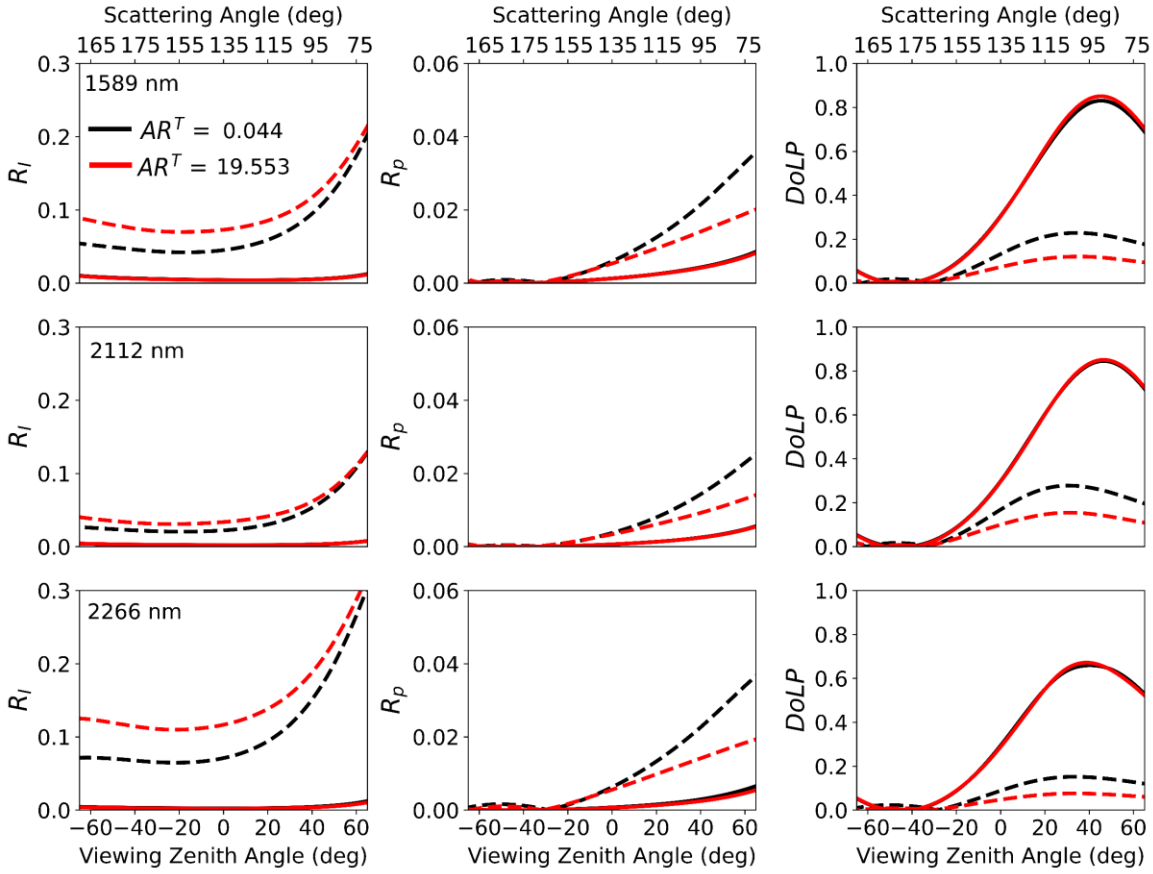

Figure 2: Sensitivity of R_I, R_p and DoLP (columns) to AR^T, for r_{eff}^T = 1280 μm (solid lines), and r_{eff}^T = 56 μm (dashed lines). The remaining parameters are D^T = 0.35, ρ^T = 0.1 g/cm^3, Z^T = 3 cm (top layer), and r_{eff}^B = 320 μm, AR^B = 1.0, D^B = 0.35, ρ^B = 0.3 g/cm^3 (bottom layer). The three rows are for the three SWIR wavelengths (1589 nm, 2112 nm and 2266 nm).

The GSA framework relies on the computation of the so-called Sobol indices (Sobol, 1990). For a model function g(X) of the *n* state variables $X_1,\ldots,X_n$ (in our case, the parameters in Table 1) which is square-integrable over a parameter space K^n, there exists a functional decomposition in terms of a Haar wavelet basis given by:

$$g(X) = g_o + \sum_{i=1}^{n} g_i(X_i) + \sum_{i<j}^{n} g_{i,j}(X_i, X_j) + \cdots + g_{1,2,\cdots,n}(X_1, X_2, \cdots, X_n) \quad (10)$$

The Haar wavelets form a basis for the space of all square integrable functions (L^2). Because the simulated reflectances are bounded and smooth over the sample space and the sample space is compact, the model functions for our simulations are

square integrable (i.e., the decomposition in Eq. (10) exists). Squaring both sides of the equation, integrating over the whole parameter space, and using the orthogonality properties of the basis, one obtains:

$$\int_{K^n} g^2(X) d\,X - g_0^2 = \sum_{s=1}^{n} \sum_{i_1<\cdots<i_s}^{n} \int_{K^n} g_{i_1,\cdots,i_s}^2 \left(X_{i_1}, \cdots X_{i_s}\right) d\,X_{i_1} \cdots dX_{i_s} \quad (11)$$

If each variable X_i is uniformly distributed over the parameter space K^n, the left-hand side exactly defines the variance of the model function g(X)

$$\int_{K^n} g^2(X) d\,X - g_0^2 = V_Y \quad (12)$$

whereas the integrals:

$$\int_{K^n} g_{i_1,\cdots,i_s}^2 \left(X_{i_1}, \cdots X_{i_s}\right) d\,X_{i_1} \cdots dX_{i_s} = V_{i_1,\cdots,i_s} \quad (13)$$

are the variances of the functions $g_{i_1,\cdots,i_s}\left(X_{i_1}, \cdots X_{i_s}\right)$. Combining the decomposition in Eq. (11) with Eqs. (12) and (13) gives the decomposition of the total variance:

$$V_Y = \sum_{i=1}^{n} V_i + \sum_{i<j}^{n} V_{i,j} + \sum_{i<j<k}^{n} V_{i,j,k} + \cdots + V_{1,\cdots,n} \quad (14)$$

Each V_i term in the first sum corresponds to the 'main-effect' contribution of the variable X_i to the model output. The $V_{i,j}$ terms quantify the pairwise interactions between X_i and X_j, the $V_{i,j,k}$ the triplet-wise interactions among X_i , X_j and X_k, and so on (Saltelli et al., 2008). Dividing both sides of Eq. (14) by the total variance one obtains:

$$1 = \sum_{i=1}^{n} S_i + \sum_{i<j}^{n} S_{i,j} + \sum_{i<j<k}^{n} S_{i,j,k} + \cdots + S_{1,\cdots,n} \quad (15)$$

where the "total-effect" Sobol index for the parameter X_j:

$$S_{T_j} = 1 - \sum_{j \notin \{i_1,\cdots,i_s\}} S_{i_1,\cdots,i_s} \quad (16)$$

quantifies the complete contribution of X_j to the total variance over the entire parameter space, both directly and through interactions among parameters. The Sobol indices are calculated at each angle with the Python software package SALib (Herman and Usher, 2017; Iwanaga et. al., 2022), which uses the quasi-Monte-Carlo estimators presented in Saltelli et. al. (2010). To compare the indices at different wavelengths, they are converted into absolute quantities by multiplying by the total variance at that angle:

$$\sigma_{T_j}^{Y} = \sqrt{S_{T_j} \cdot V_Y} \quad (17)$$

A visual interpretation of the Sobol indices is given in Fig. 3, where the grey curves show the total reflectance at 555 nm output by the radiative transfer model for twenty random combinations of input parameters, computed for a solar zenith angle (SZA) of 65°. The region shaded in blue represents the total variance of the model curves and the area in red the total-effect Sobol index $\sigma_T^{R_I}$ relative to τ_c^{555}. A comparison between $\sigma_{R_I} = \sqrt{V_{R_I}}$ and $\sigma_T^{R_I}$ reveals that a significant portion of the total variance of the model is due to variations in τ_C^{555}.

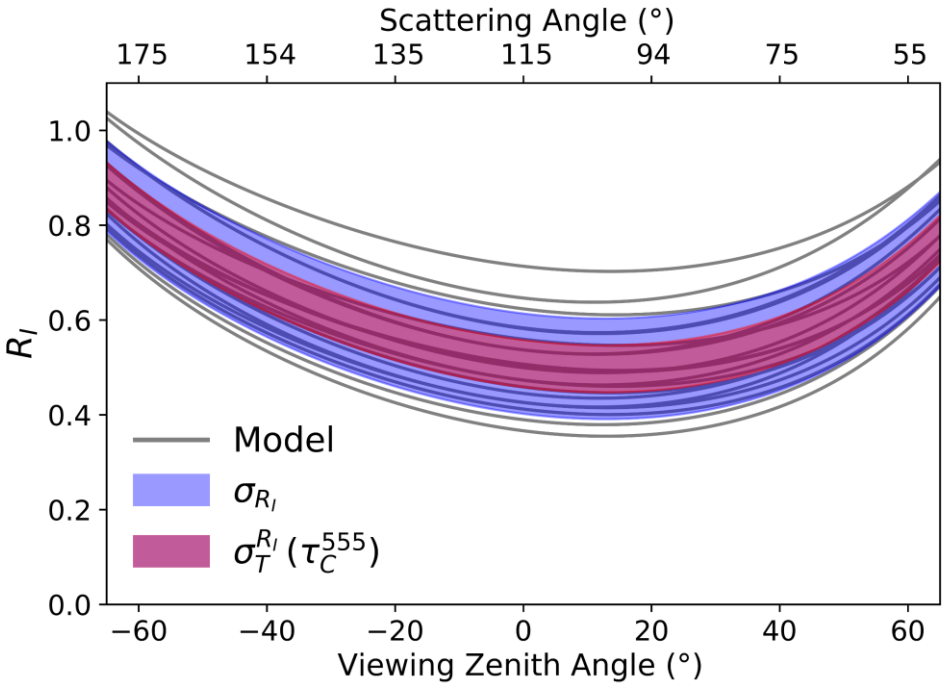

Figure 3: Total reflectance R_I (grey lines) at 555 nm simulated for 20 random combinations of the state parameters, as a function of viewing zenith angle along the principal plane (SZA=65°). The total standard deviation for this ensemble of curves σ_{R_I} is shown by the blue shaded region and the red shaded region corresponds to the absolute total effect Sobol index $\sigma_T^{R_I}$ associated with variations in τ_c^{555}. The fact that $\sigma_T^{R_I}$ covers a large portion of σ_{R_I} indicates that a large amount of the variation in R_I is due to τ_c^{555}.

The sensitivities are evaluated against the 1σ uncertainty corresponding to the square root of the diagonal elements of the measurement error covariance matrix (Knobelspiesse et al., 2012). Full measurement covariance matrices which include off-diagonal elements expressing cross-correlation effects can be hard to assess (Gao et al., 2023). In line with other studies that consider the uncertainty of multi-angle polarimeters (Hasekamp, 2010; Lebsock et al., 2007; Stamnes et al., 2018; Ottaviani et al., 2012), we also neglect such elements that in any case do not affect our main conclusions.

The light gray areas in Fig. 4 (see also discussion in the next section) correspond to a 3% (0.5%) radiometric (polarimetric) accuracy, nominally achievable by modern spaceborne sensors like the polarimeters launched onboard PACE. The dark gray areas correspond instead to the higher accuracy of RSP-like sensors (1.5% radiometric and 0.2% polarimetric). Note that the uncertainty in R_p is rather different in the two cases, since the error model used for the areas in

light gray includes a term proportional to R_I^2. This term is a result of a filter-wheel-type of design, where the measurements needed to compile the Stokes vector of any given scene are not acquired simultaneously (Dubovik et al., 2019; Knobelspiesse et al., 2012), and is large over bright surfaces as is the case for snow in the VIS-NIR.

If σ_{Ti} is less than the threshold at all angles, the associated parameter is ruled out as a meaningful contributor to model variance and is excluded from the plot. The SALib package also gives relative confidence intervals for each Sobol index, which are converted to absolute confidence intervals around σ_{Ti}. A sample size $m=2^{16}$ (specified as a power of 2 as required by the software package) was chosen for a total of $(n+1)m=1{,}048{,}575$ runs (where $n=14$ is the number of parameters), which ensures that for all σ_T curves which lie above the uncertainty threshold, the confidence interval also lies above the uncertainty threshold.

As discussed below, values of σ_{Ti} above the uncertainty threshold do not necessarily guarantee retrievability, which is impacted by model uncertainty and other sources of error unaccounted for in the covariance matrices used here. In this respect, the retrievals can be considered as a best-case scenario (Rodgers, 2000; Knobelspiesse et al., 2012).

3 Results and Discussion

3.1 Pure Snow

As a first example of the application of the GSA, in Fig. 4 we show the angular variations of the absolute total Sobol indices computed for a pure snow scene. Although such an idealized case is not commonly encountered in real-world scenarios, this exercise is useful to isolate and familiarize with the sensitivity to the parameters descriptive of the ice crystals; the effects of LAPs will then be discussed in the next section. In both cases, we consider optically semi-infinite snowpacks since the focus of this paper is on the remote sensing of snow; heterogeneous pixels constitute an added layer of complexity and will be the subject of future studies.

The results are for principal plane observations and SZA=65°. Note that the top x-axis in the first row reports the conversion to scattering angles, useful to connect scanning viewing zenith angles (VZAs) to forward and backscattering directions in the discussions that follow. The different wavelengths are in different rows, and only state parameters exhibiting sensitivity over the 1σ instrument uncertainty threshold are included. The GSA correctly captures the known dependence of the reflectance on the top-layer grain size in the SWIR (increasing with viewing zenith angle in the forward-scattering half-plane, see also Fig. 2) due to the large absorption by ice at these wavelengths (Warren and Wiscombe 1980; Dang et al. 2016), which is exploited in retrieval schemes (Stamnes et al., 2007; Painter et. al, 2009; 2003; Nolin and Dozier, 1993). The lack of sensitivity of R_I to grain size in the VIS is explained by the fact that pure snow is highly reflective (i.e. non absorbing) at visible wavelengths, which therefore are normally not used for size retrievals.

The exact penetration depth of each wavelength in the snowpack depends on grain size, snow density, and impurity content. For pure snow of typical densities and grain sizes, the VIS wavelengths penetrate deeper (10-25 cm) than NIR (3-20 cm) and SWIR (0-2 cm) wavelengths (Kokhanovsky, 2022; Libois et. al., 2013; Li et. al. 2001). Multiple scattering quickly

randomizes polarization as the incident light penetrates into a dense medium (van Diedenhoven et al., 2013), explaining why no detectable sensitivity to any of the parameters is found for R_p and DoLP in the VIS within the considered uncertainties. The situation is different in the SWIR, again because of the strong ice absorption. The very limited penetration depth allows the polarization signatures determined by the single-scattering properties of the ice crystals at the very top of the snowpack to be preserved, especially for observations of the DoLP which are typically achieved with higher measurement accuracy. Beside the evident sensitivity to r_{eff}^T and D^T in this wavelength regime, an interesting result concerns the 2266 nm RSP channel, which seems to access detectable sensitivity to AR^T not present for the nearby MODIS channel at 2112 nm. Furthermore, the reduced uncertainty of RSP-like sensors reveals sensitivity of the polarized reflectance measured at 864 nm to D^T and AR^T (Ottaviani et al., 2015).

All simulated measurements are insensitive to the mixing proportion (*f*) of columns and plates in both layers, which can be explained by the similarity of the scattering properties for crystals with reciprocal ARs (see Fig. A3). Because of its large physical thickness, the bottom layer is optically semi-infinite regardless of ρ^B. Directional changes in the light scattered downward in response to variations of D and AR do not prevent its fast extinction, and the fraction of upwelling photons supplied by the bottom layer stays pretty constant so that R_I is insensitive to ρ^B.

Finally, we note that the LUT includes random selections for the thickness of the top layer, and for the snow density in both layers. Other than for the minimal information contained in the DoLP at 2266 nm (blue and cyan curves, nearly overlapped), the Sobol indices reveal that these parameters cannot be independently retrieved. The optical depth of the top layer largely determines the observed signal but is proportional to the product of ρ^T and Z^T, which is invariant when one parameter is divided by the same factor used to multiply the other. The same argument is even more valid for the semi-infinite bottom layer, which prohibits passive optical measurements from accessing information on its thickness or density.

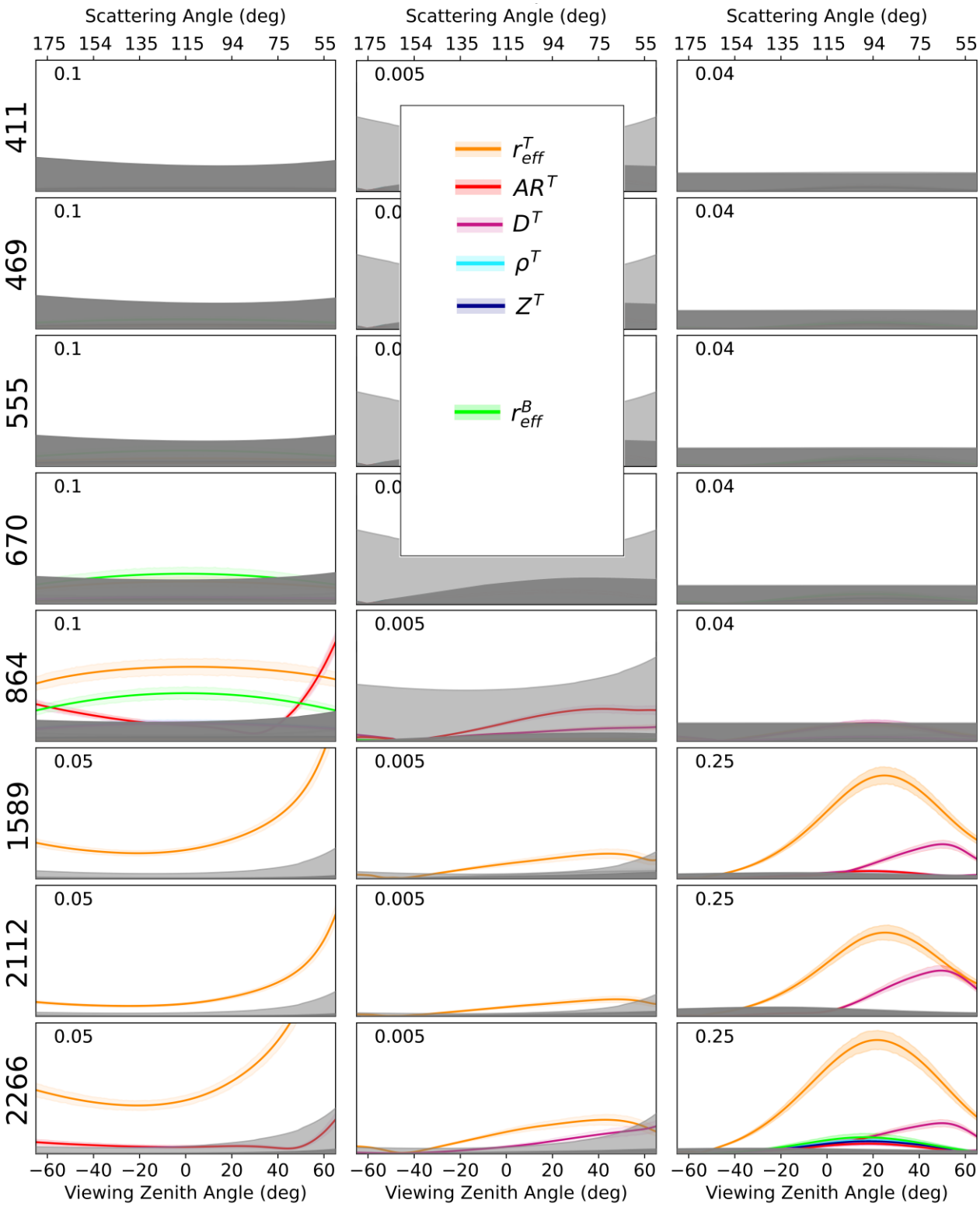

Figure 4: Absolute total Sobol index σ_T for R_I, R_p and DoLP (different columns) as a function of viewing zenith angle along the principal

plane and for SZA=65°, computed for a pure snowpack under a clear atmosphere (C_{BC}^{T} =C_{BC}^{B}=0 ppmw, τ_C^{555}= 0). The indices with their 90% confidence intervals are only given for parameters with variance above the instrument uncertainty thresholds.

The results of the GSA are particularly useful to inform on the choice of parameters to be included in the state vector of inverse retrievals. As an example, we generated synthetic TOA observations with the RT code, including random noise added according to the specifications of different sensors. As explained in Sec. 2, the snowpack consists of a mixture of crystals (f^T=f^B=0.5). Fresher snow (smaller grains) is simulated in the top layer (r_{eff}^T=150 μm, Z^T=3 cm, ρ^T=0.2 g/cm^3, AR^T=0.05 for plates and corresponding 1/AR^T=20 for columns, and D^T=0.3 as found by Ottaviani et al. (2015)). More compact, larger, and rounder grains are located in the bottom layer (r_{eff}^B=250 μm, ρ^B=0.30 g/cm^3, AR^B=0.15 for plates and 6.67 for columns, D^B=0.40), which is optically semi-infinite (τ≈2000). For the reasons given at the end of Sec. 3, the thickness of the top layer and density of both layers were not included in the set of retrievables and, together with the other parameters excluded from the state vector, are constrained to the values used to generate the synthetic observations.

Using the LMFit Python library (Newville et al., 2014), a Levenberg-Marquardt, nonlinear least-squares optimal estimation scheme (Levenberg, 1944; Marquardt, 1960) was then implemented to retrieve the input parameters. We first consider the configuration of an RSP-like instrument. In satellite imagery, every pixel is characterized by its own set of viewing zenith and azimuth angles. The RSP is instead a scanner, and we chose the principal plane as a scanning direction because it guarantees that the viewing geometries span the largest range of scattering angles.

To highlight the merits of polarization, we compare retrievals that consider as measurement vectors the simulated (i) total reflectance; (ii) total reflectance and polarized reflectance; and (iii) total reflectance and DoLP. These retrievals are repeated considering VIS, VIS+NIR or VIS+NIR+SWIR wavelengths. The SWIR combination consists of 1589 nm and 2266 nm. All available viewing angles (150 measurements for RSP, roughly between ±70°) are used for the total reflectance. Figure 4 shows that the DoLP and R_p are largely unaffected by variations in any of the parameters for angles in the backscattering half-plane. If these angles are included in the retrieval, the minimization algorithm attempts to fit very small changes in R_p or the DoLP which cannot be distinguished from the noise, and the retrieval quality degrades. Consequently, we subsampled the measurements of R_p and DoLP to positive viewing zenith angles, which in our reference system correspond to the forward scattering-half plane.

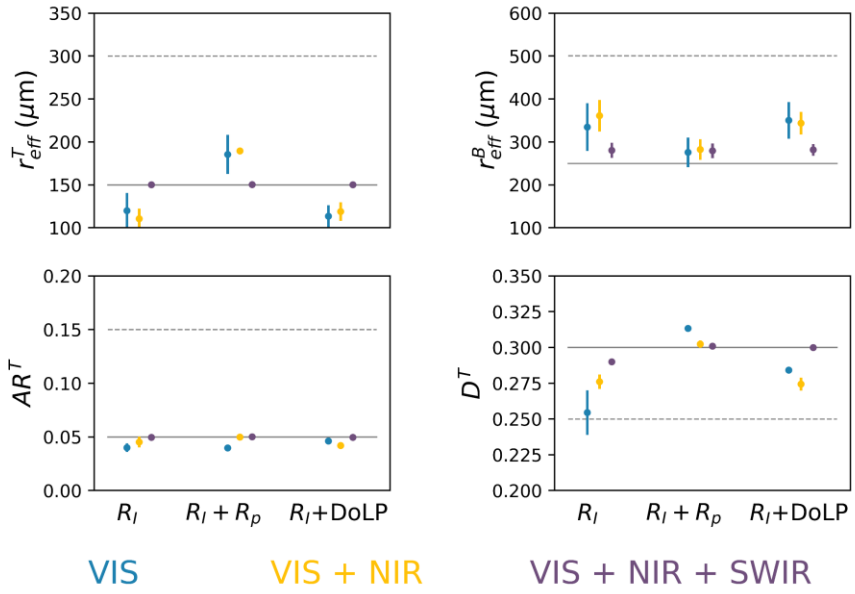

Figure 5: State parameters (different panels) retrieved from the inversion of RSP-like TOA observations, generated for SZA = 65° along the principal plane. The scene consists of a pure snowpack and a clean atmosphere (see text). The inversions are repeated with and without the inclusion of polarization and at different wavelength combinations. The solid and dashed grey lines are the "true" values and the initial guesses for each parameter.

Figure 5 summarizes the values of the state parameters and their uncertainty obtained from the inversion. The solid lines represent the "true" values used in the forward simulations. The dashed lines are instead the initial guess for each parameter, randomly sampled within the bounds listed in Table 1. The retrievals were repeated a few times to test the stability of the results against the different initial guesses.

In this simplistic scenario of a pure snowpack and a clear atmosphere, Fig. 4 indicates that R_I, R_p, and DoLP in the VIS are insensitive to all parameters (except for R_I to r_{eff}^{B} at 670 nm), and retrievals attempted with these data alone are unsuccessful. The addition of NIR measurements of R_I and R_p (if the accuracy of the latter matches RSP levels) gives access to information on grain shape and microscale roughness, as confirmed with real data (Ottaviani et al., 2012; 2015).

The retrieval becomes optimal when polarization capabilities in the SWIR are also included. Using R_I+R_p or R_I+DoLP leads to similar performances, with the inversions converging to the true values within the error bars for all parameters except for r_{eff}^{B}, which is anyway retrieved moderately well.

We next turn the attention to retrievals simulated for instruments with spectral and angular configurations different from those of the RSP. A MODIS-like sensor is mimicked by considering mono-angle measurements of total reflectance in the VIS+NIR+SWIR. The addition of 16-angle polarimetric measurements in the VIS+NIR mimics POLDER. The viewing geometries for the simulations are taken from actual data collected over Greenland for a pixel near Summit Station (72°N, 39°W) on April 8th, 2007, and for SZA ≈ 65°, which corresponds to the SZA used to generate Fig. 4. All available angular measurements are considered for the total reflectance in the VIS+NIR, subsampled to the same range as in the RSP-like case.

The results obtained using these two different instrument configurations are compared to those of the RSP in Fig. 6. Retrievals using MODIS-like data can recover the top layer grain size (Stamnes et al., 2007; Hori et al., 2007; Painter et. al, 2009; 2003; Nolin and Dozier, 1993), but fail to resolve all other parameters in a satisfactory manner. Information on grain shape is still accessible to the MODIS NIR channel, but for viewing zenith angle away from nadir. The MODIS viewing zenith angle for this particular pixel is 7°, which exemplifies the utility of multi-angular measurements. Observations of R_p contain information on D^T in the NIR, although the larger uncertainty assigned to the simulated spaceborne measurements limits the retrieval quality compared to the RSP-like case. Finally, we note that all these retrievals are robust against different choices of the initial guess for each parameter.

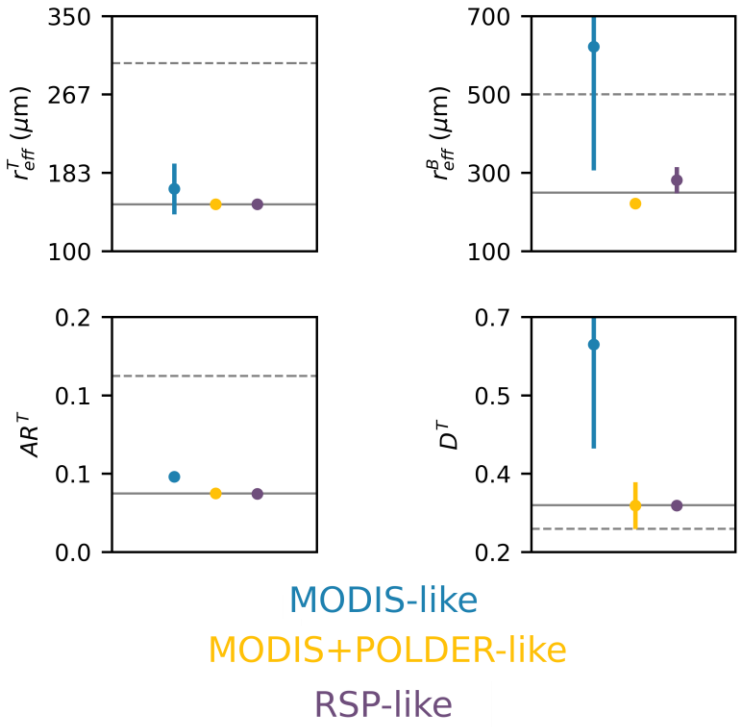

Figure 6: Similar to Fig. 5, but for inversion results of simulated MODIS-like, MODIS+POLDER-like, and RSP-like observations.

3.2 Scenes Containing Snow Impurities and Aerosols

In this section, we expand the analysis to include more realistic scenes characterized by the presence of LAPs both in the snowpack and as atmospheric aerosols. We also consider different SZAs.

Light-absorbing impurities in the snow are often found in very significant amounts in North America, China, and the Arctic (Warren, 2019). In Greenland, especially on the plateau, the concentrations are typically much smaller and therefore difficult to detect via remote sensing (Warren, 2013). Since they have anyway a significant impact on snow visible albedo (Warren, 1980; Dang, 2016), their accurate determination is especially important for climate modeling (Antwerpen et

al., 2022; Wang et al., 2020; Alexander et al., 2014; Ryan et al., 2019). To target these challenging retrievals, in Fig. 7 the results of the GSA are computed for maximum LAP loads of 0.4 for τ_c^{555} and 1 ppmw for C_{BC}^{T} and C_{BC}^{B}, where the subscript "BC" indicates the specific type of black-carbon LAP considered in this paper, with fixed microphysical and optical properties. More sporadic events like thick burning plumes or exceptionally dirty snow are addressed in the Appendix, where the same calculations are repeated with extended ranges of τ_c^{555} (up to 1.2) and C_{BC}^{T} and C_{BC}^{B} (up to 10 ppmw). At these higher LAP amounts, the sensitivity of polarimetric measurements in the SWIR to aerosol optical depth is even more pronounced (see Fig. A1 and related discussion).

The sensitivity to top- and bottom-layer parameters can be interpreted in terms of the penetration depths discussed in Sect. 3.1. The top layer thickness ranges between 1-5 cm in the LUT, explaining why the DoLP is (weakly) sensitive to r_{eff}^{B} in the SWIR at 2266 nm but not at 1589 and 2112 nm, for which the ice absorption is slightly larger.

The total reflectance in the VIS-NIR shows the expected sensitivity to LAPs. The added sensitivity to τ_c^{555} reflects the additional information provided by polarization. The fact that the polarized reflectance and the DoLP measured in the SWIR are insensitive to the concentration of LAPs in the snowpack implies that polarimetry can also be exploited to (i) extend heritage aerosol retrievals performed over other land surfaces to snow surfaces; and (ii) inform on the vertical partitioning of LAPs between the atmosphere and the surface (Ottaviani, 2022).

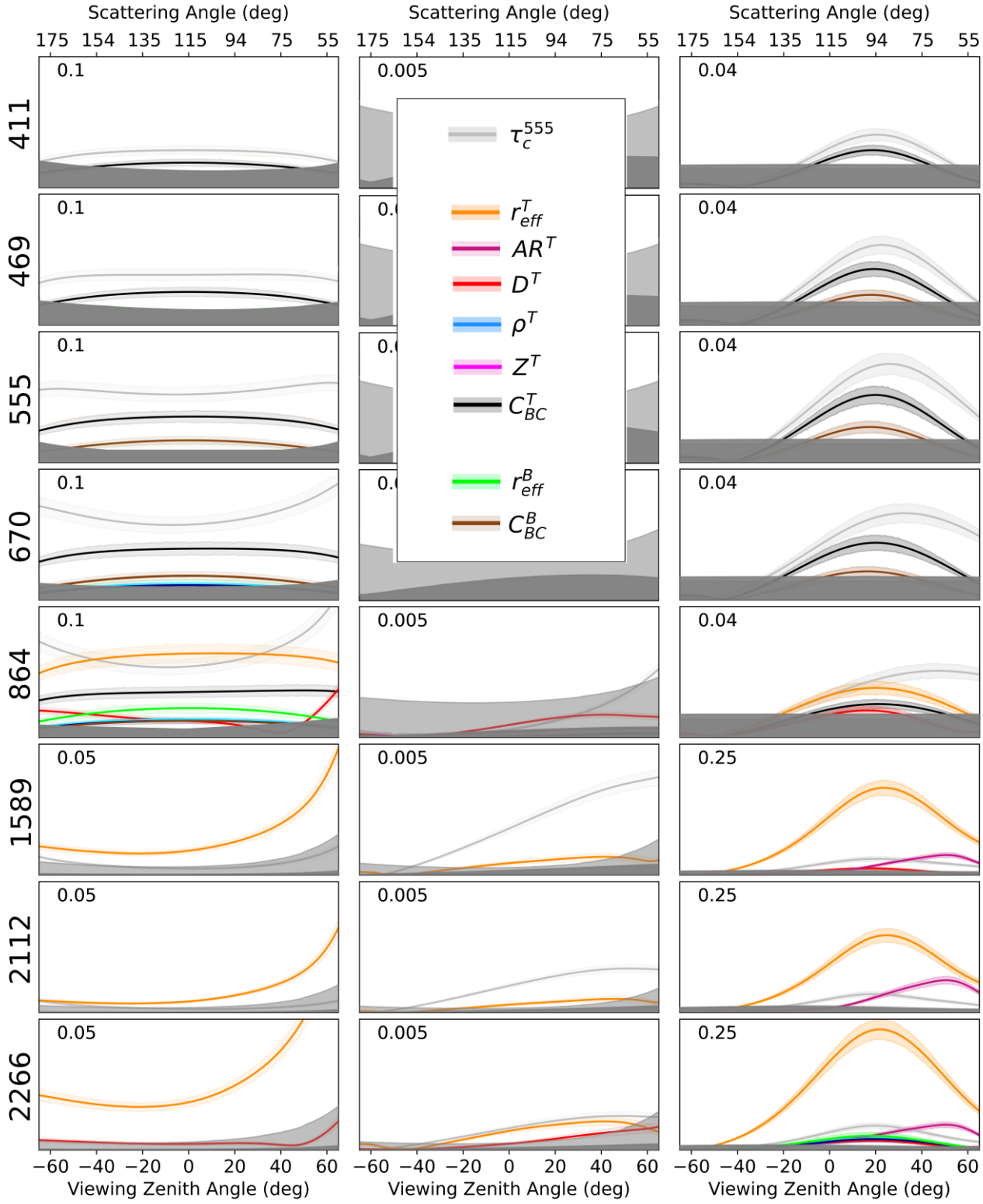

Figure 7: Same as Fig. 4, but for variable amounts of LAPs within the snowpack and in the atmosphere above.

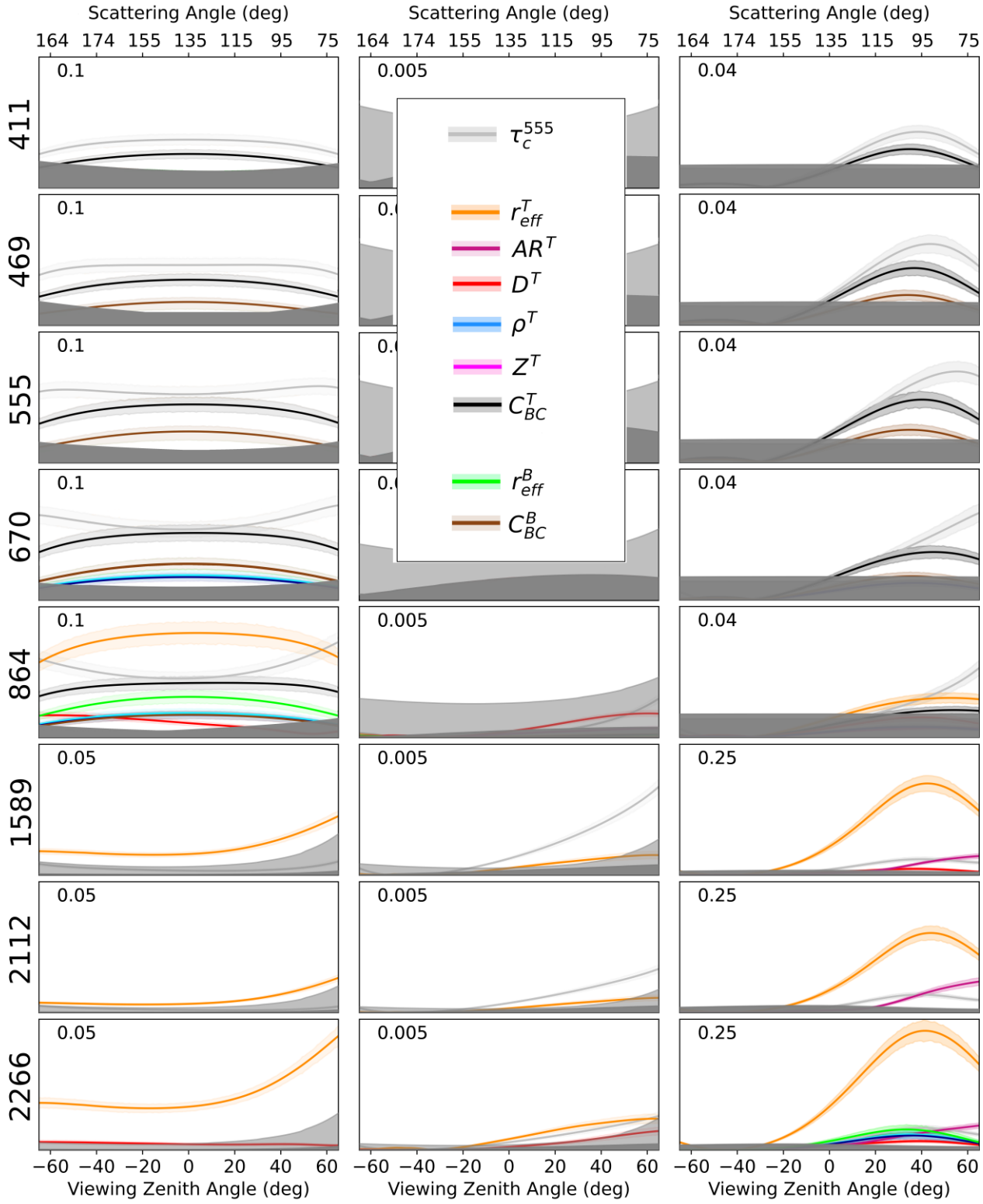

Figure 8: Same as in Fig. 7, but for a solar zenith angle of 45°.

To examine the dependence on solar illumination, Fig. 8 was produced for SZA=45°. At this smaller SZA, the angles of maximum σ_T^{DoLP} shift toward larger viewing angles. Additionally, $\sigma_T^{R_I}$ in the VIS-NIR increases for all parameters. These differences are anyway only minor; the lack of appreciable changes with SZA at least in this range typical of high latitudes is therefore attractive in the context of remote sensing applications.

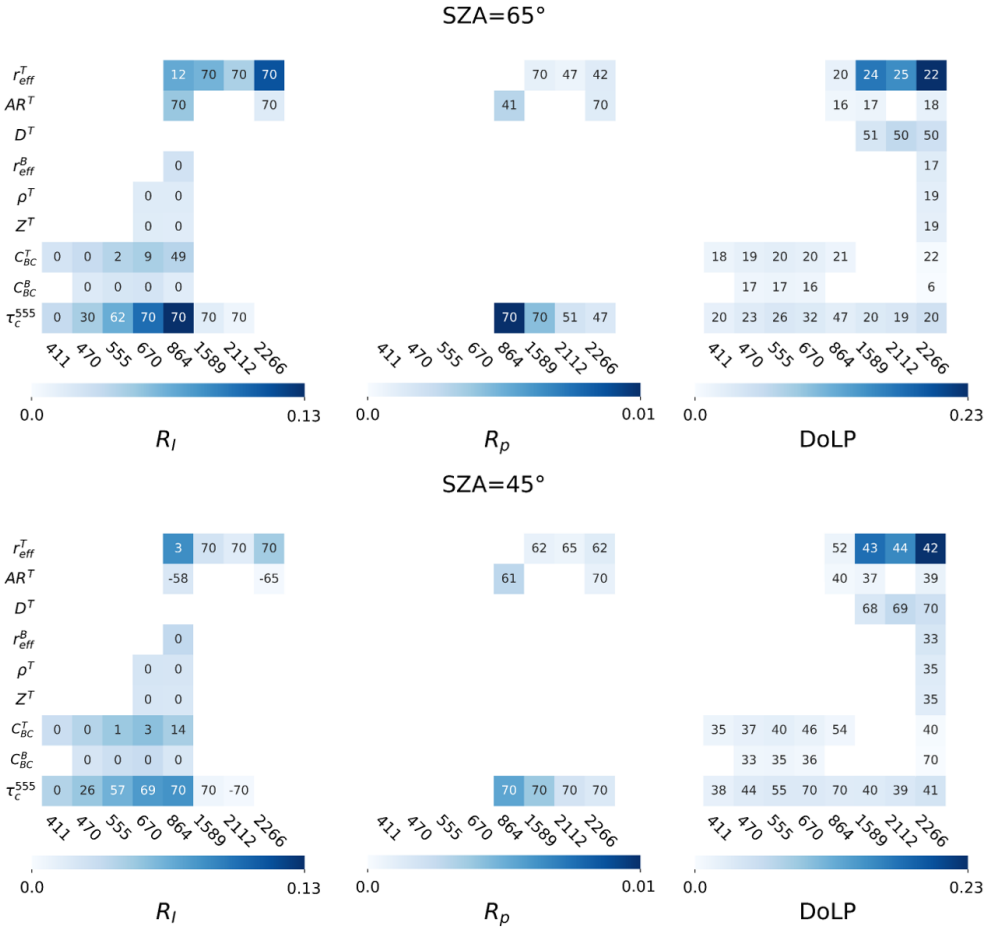

Figure 9: Heatmaps of the maximum value of $\sigma_T^{R_I}$, $\sigma_T^{R_p}$, and σ_T^{DoLP} across all viewing angles, for each parameter (row) and wavelength (column) combination. The top panel is for SZA=65° and the bottom panel for SZA=45°. The number in each box is the viewing zenith angle at which the maximum occurs. Only parameters with sensitivity over the uncertainty thresholds are included.

In the VIS-NIR, $\sigma_T^{R_I}$ exhibits an essentially flat behavior well above the detection thresholds at all viewing zenith angles for many of the parameters, with shallow maxima at around nadir except for AR^T and τ_C^{555}. In the SWIR, $\sigma_T^{R_I}$ and $\sigma_T^{R_p}$ for r_{eff}^T and τ_C^{555} peak at the largest viewing zenith angles. The DoLP includes now sensitivity to D^T, occurring still in the forward-scattering half-plane but with peaks at smaller angles. Multi-angle polarization measurements can therefore greatly supplement those of total reflectance, especially when retrieving parameters that express marked angular differences in σ_T.

Figure 9 provides an alternative display of the information contained in Figs. 7 and 8, for SZA=65° (top panel) and SZA=45° (bottom panel). These heatmaps can aid in the choice of appropriate viewing geometries and channel combinations when designing retrieval algorithms and observational strategies. The intensity of each cell's color is proportional to the maximum value of $\sigma_T^{R_I}$ (left columns), $\sigma_T^{R_p}$ (middle columns), and σ_T^{DoLP} (right columns) across all VZAs, and the number reports the angular location of these maxima. Numbers close to zero represent nadir-looking directions, and large positive angles correspond to the forward-scattering directions (see top x-axis in Figs. 7 and 8). It is evident how measurements in the forward-scattering half-plane are sensitive to the properties of aerosols and the top snow layer, while nadir-looking geometries favor the determination of parameters deeper in the snowpack. It is also clear how the addition of accurate polarimetric measurements in the VIS-SWIR benefits the retrieval of aerosol and surface properties, especially if at multiple angles.

The simulated retrievals in Sect. 3.1 were duplicated with the inclusion of LAPs. The impurity concentration in the snowpack was set to C_{BC}^{T}= C_{BC}^{B} =2.0x10^{-3} ppmw, typical of the Greenland plateau (Warren, 2019). The atmosphere contains aerosols with τ_C^{555}=0.10. Figure 10 summarizes the state parameters and their uncertainty for each type of retrieval, at different measurement vector and wavelength combinations.

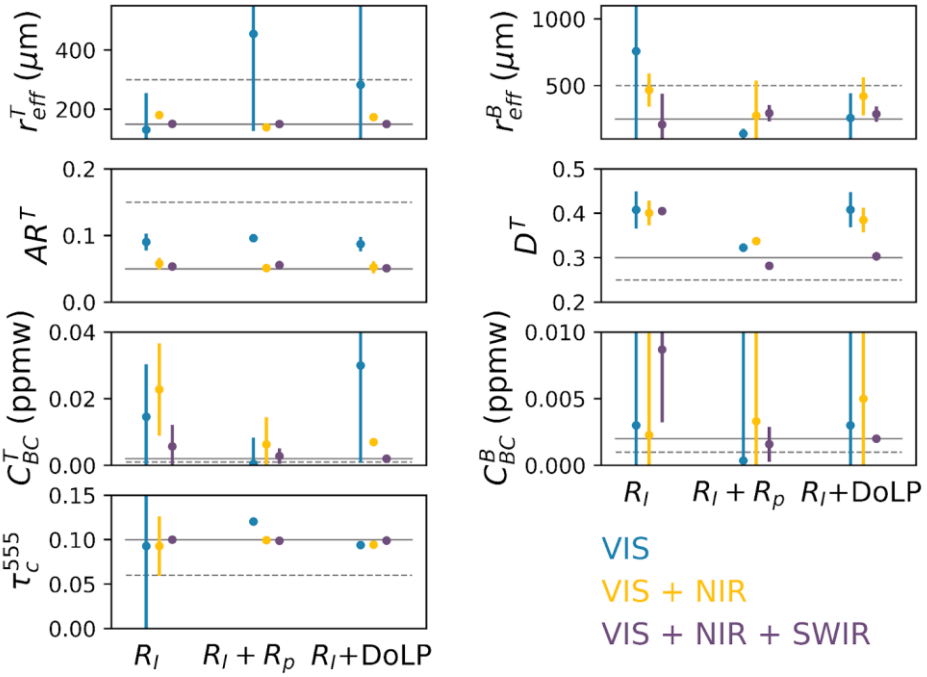

Figure 10: Same as Fig. 5, but with LAPs included in the retrievals.

Retrievals which use R_I+DoLP from only VIS and NIR channels are in general not successful and fail to distinguish between impurities in the snow and aerosols, because they are challenged by the simultaneous sensitivity to multiple parameters. Improvements are observed when measurements in the SWIR are included, due to selective sensitivity to r_{eff}^{T} and τ_C^{555}.

Unsurprisingly, the best performance is achieved by including both total reflectance and DoLP in the VIS+NIR+SWIR. The uncertainties decrease by an order of magnitude when compared to measurements of total reflectance only, confirming that polarimetric measurements in the SWIR are valuable for determining the vertical partitioning of LAPs. Initializing the inversion with first guesses close to the true values helps decreasing the uncertainty on C_{BC}^{T} and C_{BC}^{B} retrieved from the VIS+NIR+SWIR combination of R_I+R_p, but using R_I+DoLP still performs best.

We next repeat the retrievals using MODIS and MODIS+POLDER-like measurements. For the latter, we use the DoLP in the VIS-NIR in place of R_p because the DoLP manifests detectable sensitivity to LAPs. Figure 11 shows that in the MODIS-like case the inversion struggles to retrieve all parameters except r_{eff}^{T}, and the considerable uncertainties can severely impact the accuracy of derived albedo estimates. The addition of multi-angle polarimetric data enables a better determination of all parameters, even at lower angular resolution than the RSP's (Wu et al., 2015), since the angular radiative behavior of the different system components is rather smooth. One exception concerns the vertical profile of impurities in the snow: only when assuming a uniform concentration in the two layers is the retrieval successful (not shown).

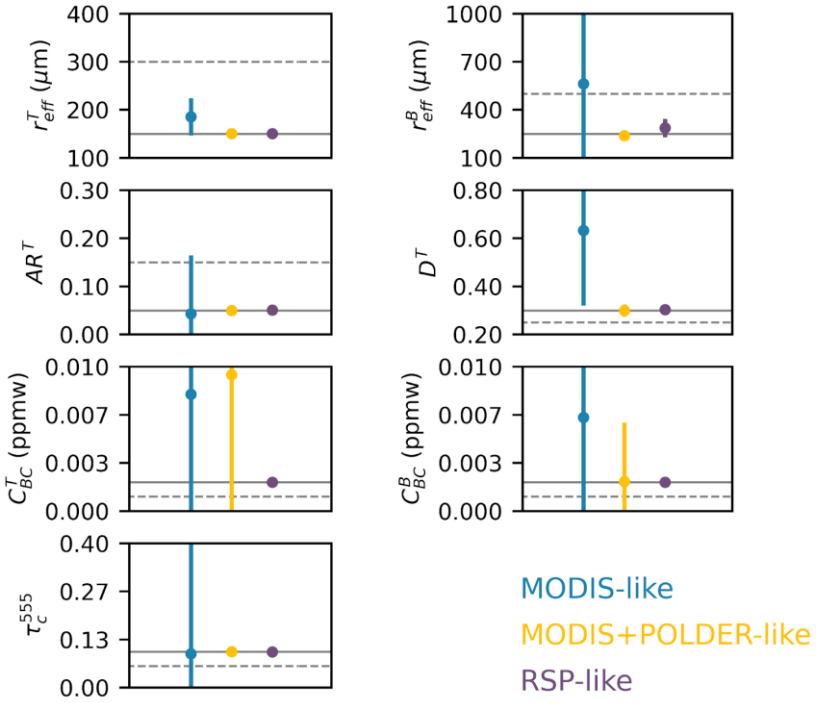

Figure 11: Same as Fig. 6, but for a scene containing LAPs in the snow and in the atmosphere.

3 Conclusions

The information content of polarimetric simulations over snow scenes was evaluated using a Global Sensitivity Analysis (GSA) method, which accounts for the correlated sensitivity to model parameters across the entire parameter space. A comprehensive look-up table (LUT) was created with an advanced vector radiative transfer model, spanning wavelengths from the VIS to the SWIR. The snow-atmosphere system is vertically resolved and accounts for the presence of light-absorbing particulates (LAPs) both embedded in and in the atmosphere above the snowpack. The Sobol indices computed from the LUT are the primary metrics for the GSA, and show the expected sensitivity of total reflectance in the VIS-NIR to LAPs and in the SWIR to snow grain size. In contrast to measurements of total reflectance only, polarimetric measurements inform on the vertical distribution of LAPs in the system thanks to differential sensitivity present especially in the SWIR. Retrievals of grain shape from polarimetric measurements in the NIR can be improved by the addition of SWIR channels, leading to better estimates of the asymmetry parameter and, in turn, of the albedo in climate models. The angular dependence of the sensitivity (especially of the DoLP) emphasizes the advantages of exploiting sensors with multi-angular capabilities. The findings are largely independent of the solar zenith angle at least at high latitudes, an additional advantage for remote sensing applications.

The information content analysis was used to inform on the choice of state parameters to be retrieved in sample Levenberg-Marquardt inversions, which were tested on synthetically generated polar scenes for different instrument configurations. The retrievals indeed confirm that mono-angle measurements of total reflectance in the VIS-SWIR (à la MODIS) can adequately resolve the grain size in the top layer, while access to more complex descriptors for the snow grains (in our case the aspect ratio and microscale roughness of hexagonal prisms) is achieved by the addition of multi-angle, polarimetric measurements in the NIR-SWIR. Such observations also make available it possible to differentiate LAPs in the snow from absorbing aerosol layers, a task that can improve the characterization of processes like aerosol deposition in climate models and, again, albedo simulations.

The findings generally promote the use of the DoLP over the polarized reflectance, and indicate that observations from the VIS all the way to the SWIR minimize the uncertainties when attempting to distinguish impurities in snow from absorbing aerosols. The GSA can be extended to LUTs that consider a whole suite of aerosol optical properties, region-specific impurity amounts and more elaborate mixing schemes (Tanikawa et al. 2019), or optically thin snowpacks with different underlying land cover types. However, the methods and results outlined in this paper provide cryospheric scientists with guidelines for selecting appropriate viewing geometries during data collection, and for the development of advanced retrieval algorithms applied to airborne and spaceborne data over snow. This perspective is particularly exciting considering the higher accuracies enabled by recent technological progress, like those of the polarimeters on PACE and 3MI.

Appendix

This Appendix discusses a few aspects that could not be included directly in the main text of the paper without unnecessarily interrupting the flow.

Figure A1 is the same as Fig. 7, but considers a larger range of aerosol optical depth (up to 1.2) and impurity density (up to 10 ppmw), which can occur as a result of burning biomass plumes or extremely "dirty" snow. With higher concentrations of LAPs, the absolute Sobol indices for the visible and NIR wavelengths increase (see Eq. 17) because BC absorption causes large variations in the total reflectance and, to a more limited extent, in the polarized reflectance especially at larger viewing zenith angles (see also Fig. 3 in Ottaviani (2022)). Larger DoLP signals also lead to a minor increase in the uncertainty threshold, but the list of parameters with identified sensitivity in Fig. 7 remains the same.

A curious aspect concerns the growing sensitivity to r_{eff}, as the concentration of snow impurities increases, as shown with the sensitivity studies performed over specific "slices" of the LUT in Fig. A2. Size measurements are achieved by exploiting absorption. Pure snow is highly reflective in the VIS-NIR, and these wavelengths cannot be exploited to retrieve the effective radius of the snow grains since, as shown by the solid lines. However, for high concentrations of impurities in the snowpack, the total reflectance and DoLP in the VIS-NIR do show dependence on r_{eff}^{T} (dashed lines). The reason for this behavior is that the impurities in the model are externally mixed in snow (Tanikawa et al., 2019) and occupy the empty spaces between grains; the absorption occurring in these negative spaces is therefore partly correlated with the dimension of the crystals.

The differences in the Sobol indices compared to Fig. 7 are only minor. Polarimetric measurements in the SWIR show selective sensitivity to τ_c^{555}, r_{eff}^{T} and D^{T}, and the sensitivity to τ_c^{555} is even more prominent. The general conclusions drawn in the main text remain therefore unaffected if a larger range of LAPs is considered.

As reported in Sec. 3, the GSA finds no sensitivity to the columns-to-plates fraction for mixtures of columns with aspect ratio AR and plates with aspect ratio 1/AR. This fact is explained by the very similar asymmetry parameters of grains with reciprocal aspect ratios (van Diedenhoven et al., 2014a), as shown in Fig. A3 for columns with $AR^{T} = 19.553$ (black) and plates with $AR^{T} = 1/19.553 = 0.051$ (red).

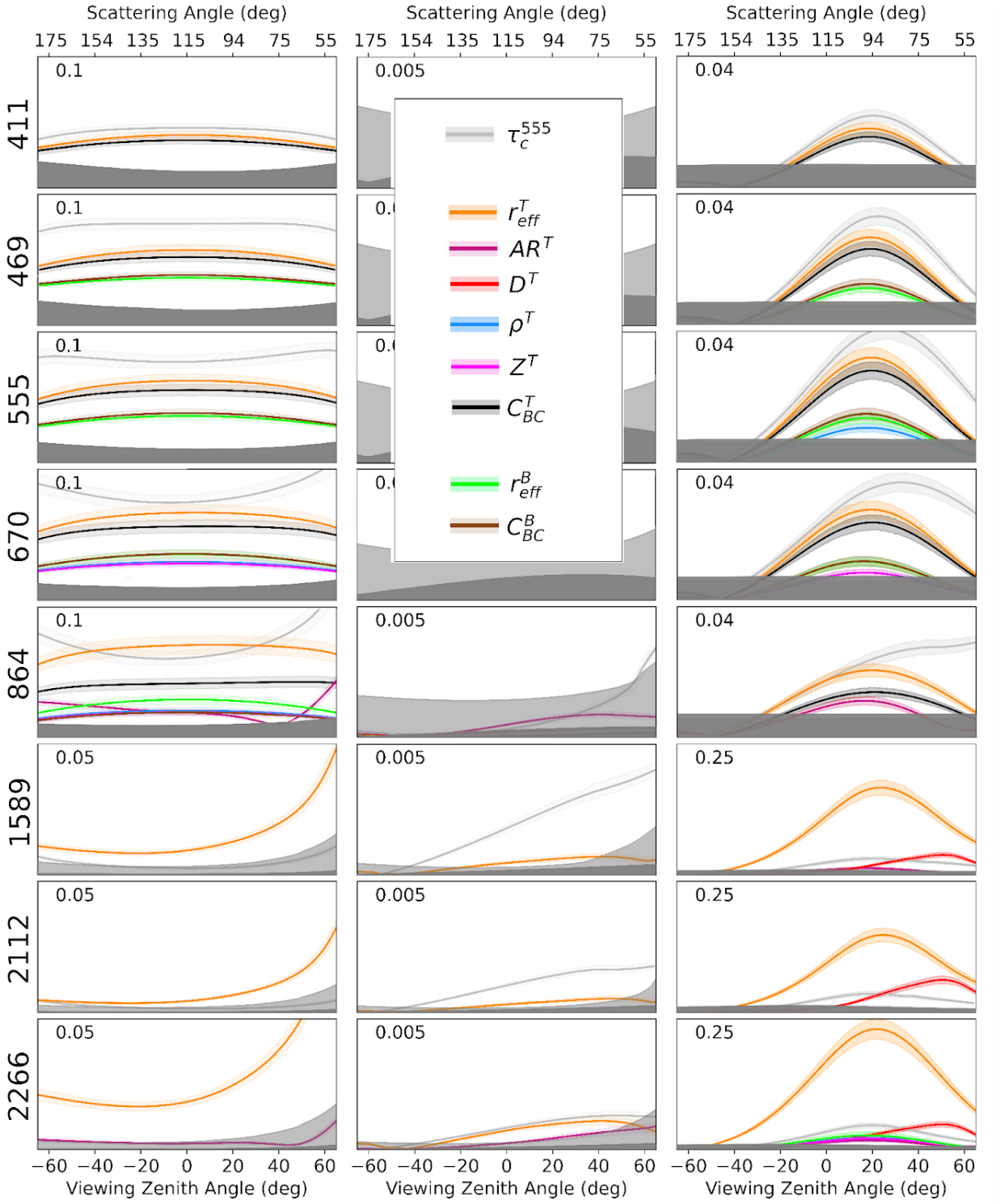

460 **Figure A1**: Same as Fig. 7, but for a larger range of aerosol optical depth (up to 1.2) and impurity density (up to 10 ppmw).

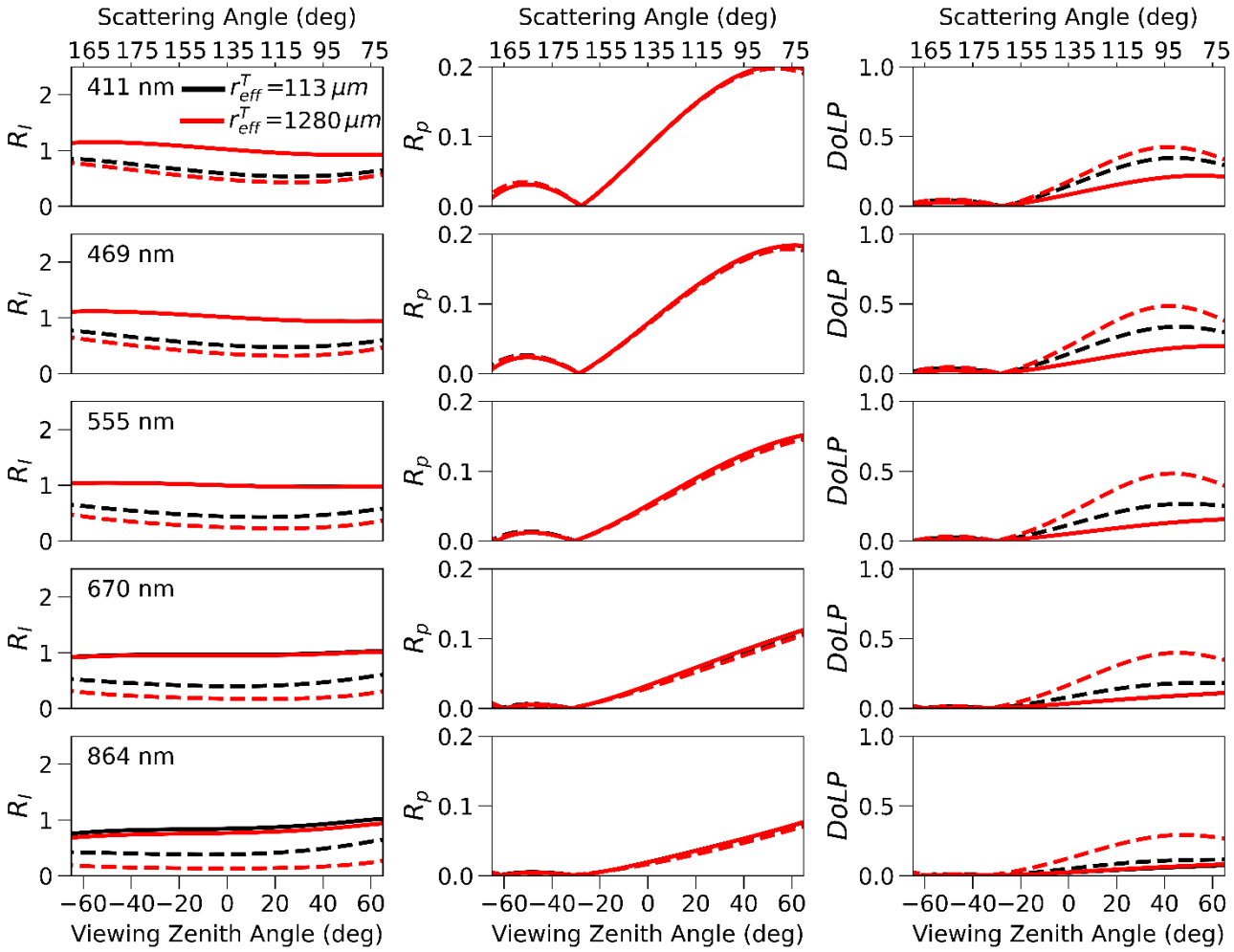

Figure A2: Sensitivity of R_I, R_p, and DoLP (columns) to r_{eff}^{T} in the VIS-NIR (rows) for pure snow (solid lines), and for snow containing impurities in top layer with C_{BC}^{T}= 5 ppmw (dashed lines). The remaining parameters are D^{T} = 0.35, ρ^{T} = 0.1 g/cm^3, Z^{T} = 3 cm, r_{eff}^{B} = 320 µm, AR^{B} = 1.0, D^{B} = 0.35, ρ^{B} = 0.3 g/cm^3, C_{BC}^{B}= 0 ppmw. Calculations are for the principal plane and SZA=65°.

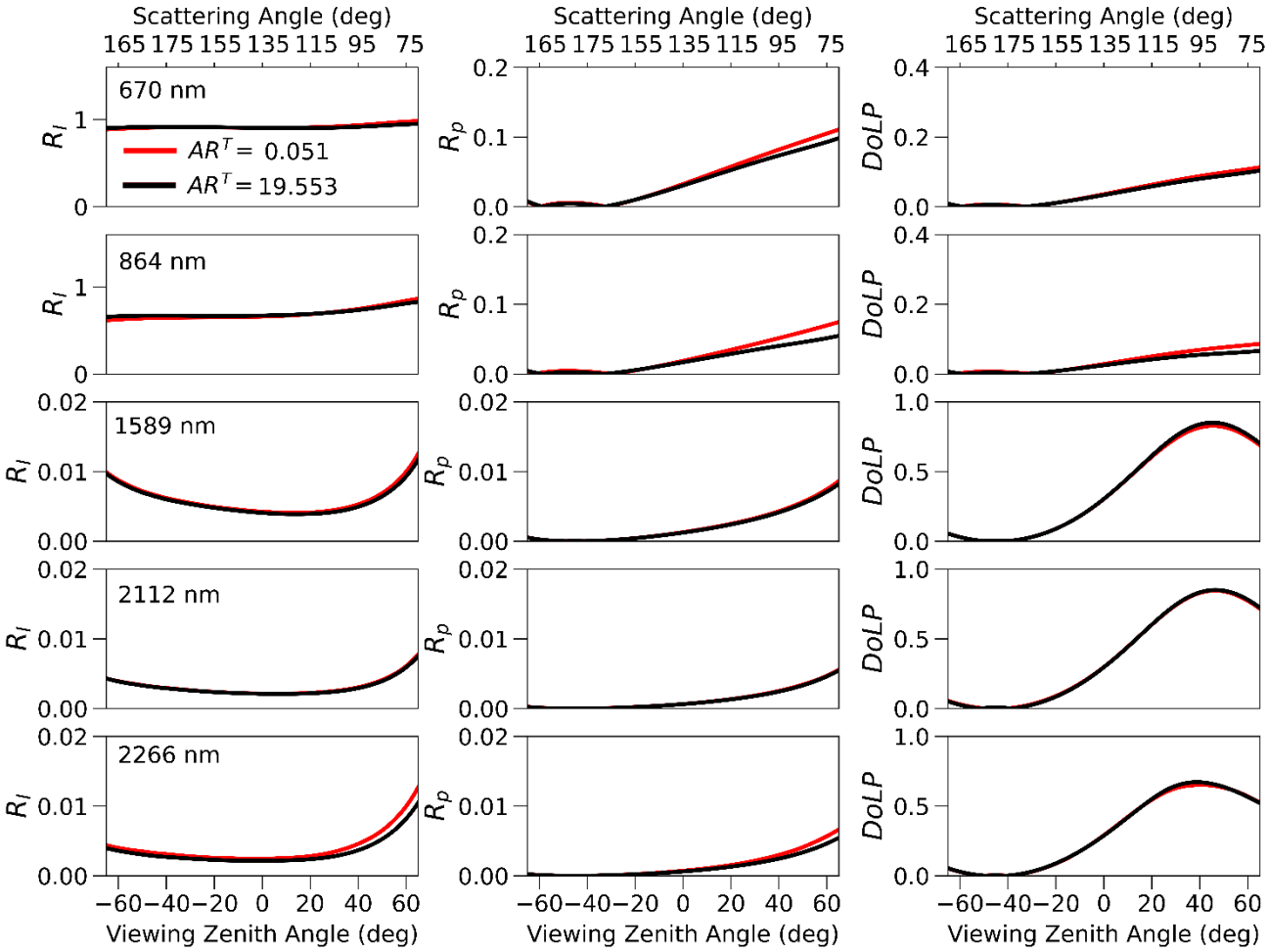

Figure A3: Comparison of R_I, R_p and DoLP (columns) for a pure snowpack consisting of column crystals with AR^T = 19.553 (red) and plate crystals with AR^T = 1 / 19.553 = 0.051 (blue) at different wavelengths (rows). The remaining parameters are fixed at r_{eff}^T = 1280 µm, D^T=D^B=0.35, ρ^T = 0.26 g/cm^3, Z^T = 3 cm, r_{eff}^B = 320 µm, AR^B = 1.0, ρ^B = 0.4 g/cm^3. Calculations are again for the principal plane and SZA=65°.

Author contributions. G.M. proposed the application of the GSA to remote sensing datasets over snow and carried out all software development and calculations. M.O., G.M., and N.C. wrote and revised the manuscript.

Competing interests. The authors declare that they have no conflict of interest.

Acknowledgements. This study was supported by the NASA award 80NSSC21K0569. G.M. gratefully acknowledges the support from the NASA Office of STEM Engagement at GISS, Minority University Research & Education Project (MUREP) & NASA OSTEM Internship program. The authors wish to thank Shenglong Wang and Valerio Luccio for their patience and guidance in configuring the supercomputing architecture provided by New York University. We also want to thank Igor Geogdzhayev at GISS for the management of the GO database of the ice crystals optical properties, and Aaditya Rangan for helpful discussions.

References

Alexander, P. M., Tedesco, M., Fettweis, X., Van De Wal, R. S. W., Smeets, C. J. P. P., and Van Den Broeke, M. R.: Assessing Spatio-Temporal Variability and Trends in Modeled and Measured Greenland Ice Sheet Albedo (2000- 2013), Cryosphere 8, 2293–2312, 2014.

Antwerpen, R. M., Tedesco, M., Fettweis, X., Alexander, P., and van de Berg, W. J.: Assessing bare-ice albedo simulated by MAR over the Greenland ice sheet (2000-2021) and implications for meltwater production estimates, The Cryosphere, 16, 4185-4199, 2022.

Aoki, T., Fukabori, M., Hachikubo, A., Tachibana, Y., and Nishio, F.: Effects of Snow Physical Parameters on Spectral Albedo and Bidirectional Reflectance of Snow Surface, J. Geophys. Res. 105, 10219–10236, 2000.

Aoki, T., Hori, M., Motoyoshi, H., Tanikawa, T., Hachikubo, A., Sugiura, K., Yasunari, T., Storvold, R., Eide, H. A., Stamnes, K., Li, W., Nieke, J., Nakajima, Y., Takahashi, F.: ADEOS-II/GLI snow/ice products — Part II: Validation results using GLI and MODIS data, Remote Sensing of Environment, Volume 111, Issues 2–3, Pages 274-290, ISSN 0034-4257, https://doi.org/10.1016/j.rse.2007.02.035, 2007.

Biron, D., Lupi, G., Montini, G., Labate, D., Bruno, U., Melfi, D., Sist, M., Zauli, F., de Leonibus, L.: METOP-SG 3MI (Multi-viewing Multi-channel Multi-polarization Imag- ing), a powerful observing mission for future operational applications, in: Proc. EUMETSAT Meteorological Satellite Conference, Vienna, Austria, 16–20 September 2013.

Bougamont, M., Bamber, J. L., Ridley, J. K., Gladstone, R. M., Greuell, W., Hanna, E., et. al.: Impact of Model Physics on Estimating the Surface Mass Balance of the Greenland Ice Sheet. Geophys. Res. Lett. 34, L17501, 2007.

Bourdelles, B., and Fily, M.: Snow grain-size determination from Landsat imagery over Terre Adelie. Antarctica, Annals of Glaciology, 17, 86−92, 1993.

Cairns, B., Russell, E. E., and Travis, L. D.: The Research Scanning Polarimeter: Calibration and ground-based measurements, Polarization: Measurement, Analysis, and Remote Sensing II, 18 Jul. 1999, Denver, Col., Proc. SPIE, 3754, 186, 1999.

Cairns, B., Waquet, F., Knobelspiesse, K., Chowdhary, J., and Deuzé, J.-L.: Polarimetric remote sensing of aerosols over land surfaces. In Satellite Aerosol Remote Sensing over Land. A.A. Kokhanovsky and G. De Leeuw, Eds., Springer-Praxis Books in Environmental Sciences, Springer, pp. 295-325, 2009.

Campolongo, F., Saltelli, A., Cariboni, J.: From screening to quantitative sensitivity analysis. A unified approach. Computer Physics Communications 182, 978-988, 2001.

Chowdhary, J., Cairns, B., Mishchenko, M., Hobbs, P., Cota, G., Redemann, J., Rutledge, K., Holben, B. and Russell, E.: Retrieval of Aerosol Scattering and Absorption Properties from Photopolarimetric Observations over the Ocean during the CLAMS Experiment. J. Atmos. Sci., 62, 1093–1117, 2005.

Colgan, W., Box, J. E., Fausto, R. S., van As, D., Barletta, V. R., and Forsberg, R.: Surface Albedo as a Proxy for the Mass Balance of Greenland's Terrestrial Ice. Geol. Surv. Denmark Greenland Bull. 31, 93–96, 2014.

Colman, R. A.: Surface albedo feedbacks from climate variability and change, J. Geophys. Res. Atmos.,118, 2827–2834, 2013.

Dang, C., Fu, Q., and Warren, S. G.: Effect of Snow Grain Shape on Snow Albedo. J. Atmos. Sci. 73, 3573–3583, 2016.

Dubovik, O., Holben, B., Eck, T. F., Smirnov, A., Kaufman, Y. J., King, M. D., Tanré, D., and Slutsker, I.: Variability of Absorption and Optical Properties of Key Aerosol Types Observed in Worldwide Locations, J. Atmos. Sci. 59, 590–608, 2002.

Dubovik, O., Li, Z., Mishchenko, M. I., Tanré, D., Karol, Y., Bojkov, B., Cairns, B., Diner, D. J., Espinosa, W. R., Goloub, P., Gu, X., Hasekamp, O., Hong, J., Hou, W., Knobelspiesse, K. D., Landgraf, J., Li, L., Litvinov, P., Liu, Y., Lopatin, A., Marbach, T., Maring, H., Martins, V., Meijer, Y., Milinevsky, G., Mukai, S., Parol, F., Qiao, Y., Remer, L., Rietjens, J., Sano, I., Stammes, P., Stamnes, S., Sun, X., Tabary, P., Travis, L. D., Waquet, F., Xu, F., Yan, C., and Yin, D.: Polarimetric remote sensing of atmospheric aerosols: Instruments, methodologies, results, and perspectives. Journal of Quantitative Spectroscopy and Radiative Transfer, Volume 224, Pages 474-511, ISSN 0022-4073, https://doi.org/10.1016/j.jqsrt.2018.11.024, 2019.

Dumont, M., Brun, E., Picard, G., Michou, M., Libois, Q., Petit, J.-R., et al.: Contribution of Light-Absorbing Impurities in Snow to Greenland's Darkening Since 2009. Nat. Geosci. 7, 509–512, 2014.

Fettweis, X., Hanna, E., Gallée, H., Huybrechts, P., and Erpicum, M.: Estimation of the Greenland Ice Sheet Surface Mass Balance for the 20th and 21st Centuries. Cryosphere 2, 117–129, 2008.

Flanner, M. G., and Zender, C. S.: Linking Snowpack Microphysics and Albedo Evolution. J. Geophys. Res. Atmosph. 111, 208, 2006.

Fu, G., Hasekamp, O., Rietjens, J., Smit, M., Di Noia, A., Cairns, B., Wasilewski, A., Diner, D., Seidel, F., Xu, F., Knobelspiesse, K., Gao, M., da Silva, A., Burton, S., Hostetler, C., Hair, J., and Ferrare, R.: Aerosol retrievals from different polarimeters during the ACEPOL campaign using a common retrieval algorithm. Atmos. Meas. Tech., 13, 553–573, 2020.

Fu, Q.: A New Parameterization of an Asymmetry Factor of Cirrus Clouds for Climate Models. J. Atmos. Sci. 64, 4140–4150, 2007.

Gao, M., Franz, B. A., Knobelspiesse, K., Zhai, P.-W., Martins, V., Burton, S., Cairns, B., Ferrare, R., Gales, J., Hasekamp, O., Hu, Y., Ibrahim, A., McBride, B., Puthukkudy, A., Werdell, P. J., and Xu, X.: Efficient multi-angle polarimetric inversion of aerosols and ocean color powered by a deep neural network forward model. Atmos. Meas. Tech., 14, 4083–4110, 2021.

Gao, M., Franz, B. A., Zhai, P.-W., Knobelspiesse, K., Sayer, A., Xu, X., Martins, V., Cairns, B., Castellanos, P., Fu, G., Hannadige, N., Hasekamp, O., Hu, Y., Ibrahim, A., Patt, F., Puthukkudy, A., and Werdell, P. J.: Simultaneous retrieval of aerosol and ocean properties from PACE HARP2 with uncertainty assessment using cascading neural network radiative transfer models, EGUsphere [preprint], https://doi.org/10.5194/egusphere-2023-1843, 2023.

Geogdzhayev, I.V., and B. van Diedenhoven.: The effect of roughness model on scattering properties of ice crystals., J. Quant. Spectrosc. Radiat. Transfer, 178, 134-141, 2016.

Hansen, J., and Nazarenko, L.: Soot Climate Forcing via Snow and Ice Albedos, Proc. Natl. Acad. Sci. U. S. A. 101, 423–428, 2004.

Hasekamp, O. P.: Capability of multi-viewing-angle photo-polarimetric measurements for the simultaneous retrieval of aerosol and cloud properties, Atmos. Meas. Tech., 3, 839–851, https://doi.org/10.5194/amt-3-839-2010, 2010.

Hasekamp, Otto P., Fu, Guangliang, Rusli, Stephanie P., Wu, Lianghai, Di Noia, Antonio, aan de Brugh, Joost, Landgraf, Jochen, Smit, J. Martijn, Rietjens, Jeroen, van Amerongen, Aaldert.: Aerosol measurements by SPEXone on the NASA

PACE mission: expected retrieval capabilities, Journal of Quantitative Spectroscopy and Radiative Transfer, Volume 227, 2019, Pages 170-184, ISSN 0022-4073, 2018.

He, C., Liou, K.-N., Takano, Y., Yang, P., Qi, L., & Chen, F.: Impact of grain shape and multiple black carbon internal mixing on snow albedo: Parameterization and radiative effect analysis. Journal of Geophysical Research: Atmospheres, 123, 1253– 1268, 2018.

Herman, J. and Usher, W.: SALib: An open-source Python library for sensitivity analysis, Journal of Open Source Software, 2(9), 2017.

Hori, M., Aoki, T., Stamnes, K., Li, W.: ADEOS-II/GLI snow/ice products — Part III: Retrieved results, Remote Sensing of Environment, Volume 111, Issues 2–3, Pages 291-336, ISSN 0034-4257, https://doi.org/10.1016/j.rse.2007.01.025, 2007.

Iwanaga, T., Usher, W., & Herman, J.: Toward SALib 2.0: Advancing the accessibility and interpretability of global sensitivity analyses, Socio-Environmental Systems Modelling, 4, 2022.

Jin, Z., Charlock, T., Yang, P., Xie, Y., and Miller, W.: Snow Optical Properties for Different Particle Shapes with Application to Snow Grain Size Retrieval and MODIS/CERES Radiance Comparison Over Antarctica, Remote Sens. Environ. 112, 3563–3581, 2008.

Kawata, Y.: Circular polarization of sunlight reflected by planetary atmospheres, Icarus 33, 217–232, 1978.

Khan, A. L., Xian, P., and Schwarz, J. P.: Black carbon concentrations and modeled smoke deposition fluxes to the bare-ice dark zone of the Greenland Ice Sheet, The Cryosphere, 17, 2909–2918, 2023.

Knobelspiesse, K., B. Cairns, M. Mishchenko, J. Chowdhary, K. Tsigaridis, B. van Diedenhoven, W. Martin, M. Ottaviani, and M. Alexandrov.: Analysis of fine-mode aerosol retrieval capabilities by different passive remote sensing instrument designs. Opt. Express, 20, 21457-21484, 2012.

Kokhanovsky, A.: Light penetration in snow layers, Journal of Quantitative Spectroscopy and Radiative Transfer, Volume 278, 108040, ISSN 0022-4073, 2022.

Kokhanovsky, A.A., Davis, A.B., Cairns, B., Dubovik, O., Hasekamp, O.P., Sano, I., Mukai, S., Rozanov, V.V., Litvinov, P., Lapyonok, T., Kolomiets, I.S., Oberemok, Y.A., Savenkov, S., Martin, W., Wasilewski, A., Di Noia, A., Stap, F.A.,

Rietjens, J., Xu, F., Natraj, V., Duan, M., Cheng, T., Munro, R.: Space-based remote sensing of atmospheric aerosols: The multi-angle spectro-polarimetric frontier. Earth-Science Reviews, Volume 145, Pages 85-116, ISSN 0012-8252, 2015.

Kokhanovsky, A., Rozanov, V., Aoki, T., Odermatt, D., Brockmann, C., Krüger, O., et al.: Sizing Snow Grains Using Backscattered Solar Light, Int. J. Remote Sens. 32, 6975–7008, 2011.

Kramer, Herbert J: Observation of the Earth and Its Environment: Survey of Missions and Sensors, Berlin, Germany: Springer Science+Business Media, ISBN 3-540-42388-5, 2002.

Lebsock, M. D., L'Ecuyer, T. S., and Stephens, G. L.: Information content of near-infrared spaceborne multiangular polarization measurements for aerosol retrievals, J. Geophys. Res., 112, D14206, doi:10.1029/2007JD008535, 2007.

Levenberg, K.: A Method for the Solution of Certain Non-Linear Problems in Least Squares. Quarterly of Applied Mathematics. 2 (2): 164–168, 1944.

Li, W., Stamnes, K., Chen, B., & Xiong, X.: Retrieval of the depth dependence of snow grain size from near-infrared radiances at multiple wavelengths. Geophysical Research Letters, 28, 1699−1702, 2001.

Libois, Q., Picard, G., France, J., Arnaud, L., Dumont, M., Carmagnola, C., et al.: Influence of Grain Shape on Light Penetration in Snow, Cryosphere 7, 1803–1818. doi:10.5194/tc-7-1803-2013, 2013.

Macke, A., Mueller, J., and Raschke, E.: Single Scattering Properties of Atmospheric Ice Crystals, J. Atmos. Sci. 53, 2813–2825, 1996.

Marbach, T., Phillips, P., Lacan, A., Schlüssel, P.: The Multi-Viewing, -Channel, -Polarisation Imager (3MI) of the EUMETSAT Polar System - Second Generation (EPS-SG) dedicated to aerosol characterization, Proc. SPIE 8889, Sensors, Systems, and Next-Generation Satellites XVII, 88890I, 2013.

Marquardt, D.: An Algorithm for Least-Squares Estimation of Nonlinear Parameters, SIAM Journal on Applied Mathematics. 11 (2): 431–441, 1963.

McBride, B. A., Martins, J. V., Cieslak, J. D., Fernandez-Borda, R., Puthukuddy, A., Xu, X., Sienkiewicz, N., Cairns, B., and Barbosa, H. M. J.: Pre-launch calibration and validation of the Airborne Hyper-Angular Rainbow Polarimeter (AirHARP) instrument, EGUsphere [preprint], 2023.

Newville, M., Stensitzki, T., Allen, D. B., & Ingargiola, A.: LMFIT: Non-Linear Least-Square Minimization and Curve-Fitting for Python (0.8.0), Zenodo, 2014

Nicolaus, M, et al.: Overview of the MOSAiC expedition: Snow and sea ice, Elem Sci Anth, 10: 1, 2022.

Nolin, A. W., Dozier, J.: Estimating snow grain size using AVIRIS data. Remote Sensing of Environment, Volume 44, Issues 2–3, Pages 231-238, ISSN 0034-4257,https://doi.org/10.1016/0034-4257(93)90018-S, 1993.

Ottaviani, M.: Polarization as a Discriminator of Light-Absorbing Impurities in or Above Snow, Front. Remote Sens., 06 June 2022 Sec. Multi- and Hyper-Spectral Imaging, 2022.

Ottaviani, M., Cairns, B., Rogers, R.R., and Ferrare, R.: Iterative atmospheric correction scheme and the polarization color of alpine snow, J. Quant. Spectrosc. Radiat. Transfer, 113, 789-804, 2012.

Ottaviani, M., van Diedenhoven, B., and Cairns, B.: Photopolarimetric retrievals of snow properties, The Cryosphere, 9, 1933-1942, 2015.

Painter, T. H., Dozier, J., Roberts, D. A., Davis, R. E., Green, R. O.: Retrieval of subpixel snow-covered area and grain size from imaging spectrometer data, Remote Sensing of Environment, Volume 85, Issue 1, Pages 64-77, ISSN 0034-4257, https://doi.org/10.1016/S0034-4257(02)00187-6, 2003.

Painter, T. H., Rittger, K., McKenzie, C., Slaughter, P., Davis, R. E., Dozier, J.: Retrieval of subpixel snow covered area, grain size, and albedo from MODIS, Remote Sensing of Environment, Volume 113, Issue 4, Pages 868-879, ISSN 0034-4257, https://doi.org/10.1016/j.rse.2009.01.001, 2009.

Rae, J., Aðalgeirsdóttir, G., Edwards, T., Fettweis, X., Gregory, J., Hewitt, H., et al.: Greenland Ice Sheet Surface Mass Balance: Evaluating Simulations and Making Projections with Regional Climate Models. Cryosphere 6, 1275–1294, 2012.

Räisänen, P., Makkonen, R., Kirkevåg, A., and Debernard, J. B.: Effects of Snow Grain Shape on Climate Simulations: Sensitivity Tests with the Norwegian Earth System Model, Cryosphere 11, 2919–2942, 2017.

Rodgers, C. D.: Inverse Methods for Atmospheric Sounding: Theory and Practice. World Scientific, 240 pp, 2000.

Ryan, J.C., Smith, L.C., van As, D., Cooley, S.W., Cooper, M.G., Pitcher, L.H., and Hubbard, A.: Greenland ice sheet surface melt amplified by snowline migration and bare ice exposure. Science Advances, 5, eaav3738, 2019.

Saltelli, A., Annoni, P., Azzini, I., Campolongo, F., Ratto, M., Tarantola, S.: Variance based sensitivity analysis of model output. Design and estimator for the total sensitivity index, Computer Physics Communications 181, Issue 2, https://doi.org/10.1016/j.cpc.2009.09.018, 2010.

Saltelli, A., M. Ratto, T. Andres, F. Campolongo, J. Cariboni, D. Gatelli, and S. Tarantola: Global Sensitivity Analysis: The Primer, JohnWiley, Chichester, U. K, 2008.

Sobol, I. M.: Sensitivity estimates for nonlinear mathematical models. Matematich-eskoe Modelirovanie, 112–118, 1990.

Stamnes K., Li W., Eide H., Aoki T., Hori M., Storvold R.: ADEOS-II/GLI snow/ice products — Part I: Scientific basis, Remote Sensing of Environment, Volume 111, Issues 2–3, https://doi.org/10.1016/j.rse.2007.03.023, 2007.

Stamnes, S., Hostetler, C., Ferrare, R., Burton, S., Liu, X., Hair, J., Hu, Y., Wasilewski, A., Martin, W., van Diedenhoven, B., Chowdhary, J., Cetinić, I., Berg, L. K., Stamnes, K., and Cairns, B.: Simultaneous polarimeter retrievals of microphysical aerosol and ocean color parameters from the "MAPP" algorithm with comparison to high-spectral-resolution lidar aerosol and ocean products, Appl. Opt. 57, 2394-2413, 2018.

Tanaka, K., Okamura, Y., Mokuno, M., Amano, T., Yoshida, J.: First year on-orbit calibration activities of SGLI on GCOM-C satellite, In: Proceedings of SPIE AsiaPacific Remote Sensing, Honolulu, Hawaii, USA. 10781 SPIE. https://doi.org/10.1117/12.2324703, 2018.

Tedesco, M., Fettweis, X., Mote, T., Wahr, J., Alexander, P., Box, J. E., and Wouters, B.: Evidence and Analysis of 2012 Greenland Records from Spaceborne Observations, a Regional Climate Model and Reanalysis Data. Cryosphere 7, 615–630. doi:10.5194/tc-7-615-2013, 2013.

Tedesco, M., and Kokhanovsky, A.: The Semi-Analytical Snow Retrieval Algorithm and its Application to Modis Data. Remote Sens. Environ. 111, 228–241. doi:10.1016/j.rse.2007.02.036, 2007.

Thackeray, C. W., Qu, X., & Hall, A.: Why do models produce spread in snow albedo feedback? Geophysical Research Letters, 45, 6223–6231. https://doi.org/10.1029/2018GL078493, 2018.

Thomas, J. L., et al.: Quantifying black carbon deposition over the Greenland ice sheet from forest fires in Canada, Geophys. Res. Lett., 44, 7965–7974, doi:10.1002/2017GL073701, 2017.

Torres, B., Dubovik, O., Fuertes, D., Schuster, G., Cachorro, V. E., Lapyonok, T., Goloub, P., Blarel, L., Barreto, A., Mallet, M., Toledano, C., and Tanré, D.: Advanced characterisation of aerosol size properties from measurements of spectral optical depth using the GRASP algorithm, Atmos. Meas. Tech., 10, 3743–3781, https://doi.org/10.5194/amt-10-3743-2017, 2017.

van Angelen, J. H., Lenaerts, J. T. M., Lhermitte, S., Fettweis, X., Kuipers Munneke, P., van den Broeke, M. R., van Meijgaard, E., and Smeets, C. J. P. P.: Sensitivity of Greenland Ice Sheet surface mass balance to surface albedo parameterization: a study with a regional climate model, The Cryosphere, 6, 1175–1186, https://doi.org/10.5194/tc-6-1175-2012, 2012.

van den Broeke, M., Smeets, C., and Van de Wal, R.: The Seasonal Cycle and Interannual Variability of Surface Energy Balance and Melt in the Ablation Zone of the West Greenland Ice Sheet. Cryosphere 5, 377–390. doi:10.5194/tc-5-377-2011, 2011.

van Diedenhoven, B., Cairns, B., Geogdzhayev, I., Fridlind, A., Ackerman, A., Yang, P., et al.: Remote Sensing of Ice Crystal Asymmetry Parameter Using Multi-Directional Polarization Measurements - Part 1: Methodology and Evaluation with Simulated Measurements. Atmos. Meas. Tech. 5, 2361–2374. doi:10.5194/amt-5-2361-2012, 2012.

van Diedenhoven, B., Cairns, B., Fridlind, A. M., Ackerman, A. S., and Garrett, T. J.: Remote sensing of ice crystal asymmetry parameter using multi-directional polarization measurements – Part 2: Application to the Research Scanning Polarimeter, Atmos. Chem. Phys., 13, 3185–3203, doi:10.5194/acp-13-3185- 2013, 2013.

van Diedenhoven, B., Ackerman, A. S., Cairns, B., and Fridlind, A. M.: A Flexible Parameterization for Shortwave Optical Properties of Ice Crystals. J. Atmos. Sci. 71, 1763–1782. doi:10.1175/jas-d-13-0205.1, 2014a.

Wang, S., Tedesco, M., Alexander, P., and Fettweis, X., Quantifying spatiotemporal variability of glacier algal blooms and the impact on surface albedo in southwestern Greenland. The Cryosphere, 14, 2687-2713, https://doi.org/10.5194/tc-14-2687-2020, 2020.

Warren, S.G.: Can Black Carbon in Snow Be Detected by Remote Sensing?, J.Geophys.Res.(Atmospheres) 118,D018476.doi:10.1029/2012jd018476, 2013.

Warren S. G.: Optical properties of ice and snow., Phil. Trans. R. Soc. A.3772018016120180161, 2019.

Warren, S. G., and Wiscombe, W.: A Model for the Spectral Albedo of Snow. II: Snow Containing Atmospheric Aerosols, J. Atmos. Sci. 37, 2734–2745. doi:10.1175/1520-0469(1980)037<2734:amftsa>2.0.co;2, 1980.

Werdell, P. J., Behrenfeld, M. J., Bontempi, P. S. et al.: The Plankton, Aerosol, Cloud, ocean Ecosystem (PACE) mission: Status, science, advances. Bulletin of the American Meteorological Society 100 (9): 1775–179, 2019.

Wu, L., Hasekamp, O., van Diedenhoven, B., and Cairns, B.: Aerosol retrieval from multiangle, multispectral photopolarimetric measurements: importance of spectral range and angular resolution, Atmos. Meas. Tech., 8, 2625–2638, https://doi.org/10.5194/amt-8-2625-2015, 2015.

Xie, Y., Yang, P., Gao, B.-C., Kattawar, G. W., and Mishchenko, M. I.: Effect of Ice Crystal Shape and Effective Size on Snow Bidirectional Reflectance. J. Quant. Spectrosc. Radiat. Transfer 100, 457–469. doi:10.1016/j.jqsrt.2005.11.056, 2006.

Zhang, Zihan, Fu, Guangliang, and Hasekamp, Otto.: Aerosol retrieval over snow using RemoTAP, Atmos. Meas. Tech., 16, 6051–6063, https://doi.org/10.5194/amt-16-6051-2023, 2023.